Research Square

Preprints are preliminary reports that have not undergone peer review.
They should not be considered conclusive, used to inform clinical practice,
or referenced by the media as validated information.

Tracking deep-time environmental stability exposes a global conservation gap

Pedro Cermeño

pedrocermeno@icm.csic.es

Centro Mediterraneo de Investigaciones Marinas y Ambientales, Consejo Superior de Investigaciones Científicas https://orcid.org/0000-0002-3902-3475

Carmen García-Comas

Instituto de Ciencias del Mar, CSIC

Gloria Herrero-Gascón

Centro Mediterraneo de Investigaciones Marinas y Ambientales, Consejo Superior de Investigaciones Científicas

Khushboo Gurung

School of Earth and Environment, University of Leeds

Guillame Le Gland

Aix-Marseille Université

Benjamin Mills

University of Leeds https://orcid.org/0000-0002-9141-0931

Alexandre Pohl

Université Bourgogne Europe https://orcid.org/0000-0003-2328-351X

Sergio Vallina

Gijon Oceanography Centre / Spanish National Research Council (CSIC) https://orcid.org/0000-0002-1335-9237

Simon Williams

University of Tasmania https://orcid.org/0000-0003-4670-8883

Biological Sciences - Article

Keywords: Plate tectonics, Climate velocity, Lagrangian framework, Macroevolution, Biogeography, Conservation

Posted Date: November 2nd, 2026

DOI: https://doi.org/10.21203/rs.3.rs-11306358/v1

License: This work is licensed under a Creative Commons Attribution 4.0 International License.
Read Full License

Additional Declarations: There is **NO** Competing Interest.

Tracking deep-time environmental stability exposes a global conservation gap

Pedro Cermeño[1*], Carmen Garcia-Comas[1], Gloria Herrero-Gascon[1], Khushboo Gurung[2], Guillaume Le Gland[3], Benjamin Mills[2], Alexandre Pohl[4], Sergio Vallina[5], Simon Williams[6]

[1]Centro Mediterráneo de Investigaciones Marinas y Ambientales, Consejo Superior de Investigaciones Científicas, Passeig Marítim de la Barceloneta 37-49, Barcelona, 08003, Spain.
[2]School of Earth and Environment, The University of Leeds, Leeds, LS2 9JT, United Kingdom.
[3]Mediterranean Institute of Oceanography, 163 avenue de Luminy, 13288 Marseille Cedex 09, France.
[4]Université Bourgogne Europe, CNRS, Biogéosciences UMR 6282, Dijon, 21000, France.
[5]Instituto Español de Oceanografía, Consejo Superior de Investigaciones Científicas, Gijón, 21000, Spain.
[6]Institute for Marine and Antarctic Studies, University of Tasmania, 20 Castray Esplanade, Battery Point, Hobart, TAS 7004, Australia.

*Corresponding author(s). E-mail(s): pedrocermeno@icm.csic.es;

Abstract

Continents drift across latitudinal climate zones that are themselves shifting as Earth's climate evolves [1–5]. The relative speed of these two motions (tectonic versus climatic velocity) determines how much climate change a given landmass experiences over geological time: where plates and climate zones move in concert, local climates can remain stable for millions of years, allowing lineages to persist and diversify. However, whether this interplay has shaped deep-time environmental stability and, in turn, present-day biodiversity patterns remains untested. Here, using a Lagrangian framework to track land parcels through 60 million years of palaeogeographic, palaeoclimatic, and palaeoproductivity reconstructions, we show that in amphibians, reptiles, birds, and mammals, species richness increases with the time a parcel has spent within a stable environmental envelope. This accumulation shows no sign of saturation, instead accelerating across nearly all combinations of taxonomic group and environment. Integrating stability along tectonic trajectories identifies modern macroevolutionary refugia (>20 Myr of cumulative stability). Of these refugia, 77.9% lack legal protection—rising to 91.5% in Asia—and just 2.1% fall within strictly protected areas. Refugia are only modestly better protected than unstable land (22.1% versus 15.8%), with over three-quarters of this difference driven by the weakest protection tiers. Having assembled while their environments moved at centimetres to metres per year, these biotas face present-day climate velocities of hundreds of metres to kilometres per year [6, 7], a kinematic debt that protecting static coordinates alone cannot address.

Keywords: Plate tectonics, Climate velocity, Lagrangian framework, Macroevolution, Biogeography, Conservation.

Main

Environmental history has long been recognised as a primary driver of macroevolutionary and biogeographic patterns [8**?** –10]. Yet explanations of biodiversity have largely rested on present-day geography or on climate history measured at fixed locations. MacArthur and Wilson's equilibrium theory of island biogeography, for example, attributes species richness to contemporary area and isolation, with extinction and immigration rates falling, respectively, as area and isolation increase [11]. Later frameworks added a temporal dimension through island ontogeny and sea-level-driven changes in island area [12, 13] and through the time-integrated area and productivity of biomes [14]. In parallel, regions of long-term climatic stability, typically quantified as low magnitude or velocity of climate change since the Last Glacial Maximum, have been linked to high endemism and the persistence of old lineages [15–18]. All of these approaches share an implicitly Eulerian (fixed-frame) perspective, they measure environmental change at fixed geographic coordinates.

Over tens of millions of years, however, the ground itself moves. Drifting at a few centimetres per year, tectonic plates carry any given land parcel hundreds to thousands of kilometres, often across climate zones. Consequently, the environmental change a parcel experiences has two components: climate changing in place, and the parcel moving through spatial climatic gradients. Palaeobiologists routinely rotate fossil occurrences into palaeocoordinates [19–21], and historical biogeography has long incorporated plate tectonics, from vicariance biogeography to phylogenetic models with time-variable dispersal [22, 23]. In both cases, however, plate tectonic reconstructions are used mainly to place occurrences in their past settings or to model changing connectivity between areas, but rarely to quantify the environmental change accumulated along a parcel's path. A Lagrangian (moving-frame) framework makes this history explicit by tracking land parcels through time. It extends the stability hypothesis to deep time and to a moving frame, casting biodiversity hotspots as products of the environmental histories landmasses accumulate as they drift.

Recent advances in plate tectonic modelling make such a Lagrangian perspective on macroevolution feasible at global scale. Full-plate reconstructions now resolve land–ocean configurations and plate boundaries continuously through deep time [24–26]. Because they model the entire plate mosaic rather than isolated continental blocks, they yield global velocity fields from which the trajectory of any location can be reconstructed. Coupling these plate motions to palaeoclimate simulations from Earth System Models yields the path of each location through climate space, linking Earth's physical dynamics to the environmental histories that shape biodiversity [27].

Here we introduce a kinematic framework for biogeography that treats Earth's lithosphere as a moving reference frame for the evolution of biodiversity. Using a time-integrated Lagrangian metric of environmental stability, we show that the interplay between continental drift and climate velocity explains global variation in terrestrial vertebrate richness beyond that explained by contemporary climate. If deep-time stability underpins present-day diversity, the most stable regions should be conservation priorities, yet most lie outside protected areas and very few are strictly protected. Many of these regions now face climate velocities that exceed the dispersal capacities of resident taxa [28–30], so their biotas risk becoming decoupled from conditions that have persisted there for millions of years. We call this mismatch kinematic debt. Like extinction debt [31], its consequences may not yet be visible, and conservation frameworks built on fixed locations and contemporary climate are not designed to detect it.

The Lagrangian shift: moving beyond static biogeography

We define a tectonic parcel as a discrete, mobile unit of Earth's surface, whose trajectory is governed by the global tectonic velocity field. Although a parcel remains physically coherent, its environmental conditions are transient, changing as it moves through shifting climatic zones and productivity gradients. We therefore expect both the diversification rate of its biota and its carrying capacity (the maximum species richness it can support) to be constrained by the conditions encountered along its path. As a result, present-day biodiversity is a path-dependent state variable that records the evolutionary history accumulated along the parcel's trajectory.

This Lagrangian approach reveals phenomena invisible to a fixed-frame, Eulerian approach. Because habitability is a property of the parcel's position within the global climate field, the

biota exists in a state of perpetual transit and adaptation governed by the interplay between tectonic velocity ($\mathbf{v}_{\text{tec}}$) and climate velocity ($\mathbf{v}_{\text{clim}}$) (see **Methods**). We formalize this relation as the kinematic lag ($\mathcal{L}$), the speed at which a lineage's thermal optimum moves away faster than the lineage can follow, either by dispersal (V_{disp}) or by adaptation of its thermal tolerance (r_{adpt}):

$$\mathcal{L} = \max\left(0, \left|\frac{(\mathbf{v}_{\text{clim}} - \mathbf{v}_{\text{tec}}) \cdot \nabla T}{|\nabla T|}\right| - \left(V_{\text{disp}} + \frac{r_{\text{adpt}}}{|\nabla T|}\right)\right)$$

The numerator of the first term is the rate of temperature change experienced by the moving parcel; dividing it by $|\nabla T|$ converts this rate into the speed at which the lineage's thermal optimum moves away along the steepest temperature gradient. Likewise, $r_{\text{adpt}}/|\nabla T|$ converts the rate of thermal adaptation into the distance per unit time a lineage effectively covers by shifting its tolerance (see **Methods** and **Extended Data Table 1** for variables and units).

A parcel's biota remains within its niche whenever $\mathcal{L} = 0$. This can occur along a continuum between two end-members. At one end, the components of $\mathbf{v}_{\text{tec}}$ and $\mathbf{v}_{\text{clim}}$ along the temperature gradient are closely aligned, so the parcel's drift directly offsets the shifting climate. For example, as the tropical belt contracted during Cenozoic cooling, a parcel drifting equatorward at a comparable rate would have kept its resident lineages in a nearly constant thermal environment despite substantial geographic movement. At the other end, the two velocities do not cancel, but the residual thermal mismatch stays within the biota's capacity to maintain its position in niche space, whether by spatial dispersal or by local adaptation.

Where $\mathcal{L} > 0$, the biota falls behind its shifting climate, and once the accumulated lag exceeds its thermal tolerance, resident lineages are pushed beyond their limits. This occurs when a parcel is nearly stationary while its climate belt migrates, and most acutely when the parcel drifts against the climatic shift. A parallel constraint operates through food resources. Where primary productivity declines along a parcel's trajectory faster than richness can adjust, carrying capacity falls below standing richness. This creates an extinction debt that persists until the biota relaxes towards a new equilibrium.

We operationalize this framework through cumulative stability, a Lagrangian metric that integrates thermal and resource continuity along each parcel's palaeogeographic trajectory (**Box 1**; **Methods**). Applying it globally, we test whether the long-term environmental histories of parcels explain the present-day richness patterns of terrestrial vertebrates, and use the metric to map modern macroevolutionary refugia.

Box 1 | Quantifying deep-time environmental stability

Our Lagrangian framework examines the interplay of continental drift, climate dynamics and resource availability under generic biological constraints. To quantify it, we introduce cumulative stability (CS), a Lagrangian metric that integrates the duration of thermal and resource continuity experienced by a parcel in tectonic transit. Evaluated at discrete time steps (Δt), CS is updated iteratively as:

$$\text{CS}_i(t) = \text{CS}_i(t - \Delta t)\, R_i(t) + S_i(t)\, \min\left(1, \frac{B_i(t - \Delta t)}{B_{\text{thresh}}}\right) \Delta t,$$

with three components:

- **Instantaneous thermal stability (S_i):** Quantifies the thermal mismatch generated by the divergence of tectonic and climate velocities. It decays exponentially with the ratio of the temperature change experienced by the moving parcel over a time step ($|\Delta T_i(t)|$, computed along its palaeogeographic trajectory) to a representative thermal niche breadth ($\Delta T_{\text{breadth}}$):

  $$S_i(t) = \exp\left(-k_T \frac{|\Delta T_i(t)|}{\Delta T_{\text{breadth}}}\right),$$

  where k_T is a thermal sensitivity constant. Because dispersal and adaptation rates cannot be estimated globally, k_T and $\Delta T_{\text{breadth}}$ jointly represent the biota's capacity to buffer thermal change.

- **Resource retention factor (R_i):** Sets the fraction of previously accumulated stability carried forward across a time step. It depends on the relative decline in vegetation biomass density (B) over the step, $\delta_i(t) = -\Delta B_i(t)/B_i(t - \Delta t)$, beyond a resilience tolerance ρ:

  $$R_i(t) = \exp\left(-k_R \max\left(0,\ \delta_i(t) - \rho\right)\right),$$

where k_R is a resource sensitivity constant. When biomass is stable (i.e., increases or declines by less than ρ), R_i equals 1 and accumulated stability is fully retained; larger declines discount it exponentially.

- **Ecological capacity limit [$\min(1, B_i(t - \Delta t)/B_{\mathbf{thresh}})$]:** Imposes an energetic constraint on stability accumulation, where B_{thresh} is a fixed fraction of Cenozoic vegetation biomass, representing the minimum resource density required to sustain stable ecosystems. This term reduces accumulation in barren regions and caps the contribution at 1.

Reported CS values are ensemble means across 100,000 combinations of k_T, $\Delta T_{\text{breadth}}$, k_R, ρ and B_{thresh} (**Methods**).

Deep-time stability and macroevolutionary refugia

By coupling a global plate tectonic model with palaeoclimate and palaeovegetation simulations over the last 60 Myr, sampled at 5-Myr intervals (**Methods**), we tracked individual land parcels along their palaeogeographic trajectories. Sampling temperature along each trajectory yields the signed thermal mismatch, the rate at which a parcel's thermal environment changed as it moved (**Fig. 1**). This rate is the net outcome of two velocities: that at which isotherms migrate and that at which the parcel itself moves (**Extended Data Fig. 1**). During the early Cenozoic (60–50 Ma), thermal mismatch remained weak across the major continental plates. This likely reflects the reduced equator-to-pole temperature gradients of the early Eocene greenhouse [5]. From the mid-Eocene, it increased markedly with the onset of Cenozoic cooling, with widespread negative rates persisting into the late Cenozoic, predominantly where plate motion opposed isotherm displacement (**Fig. 1**).

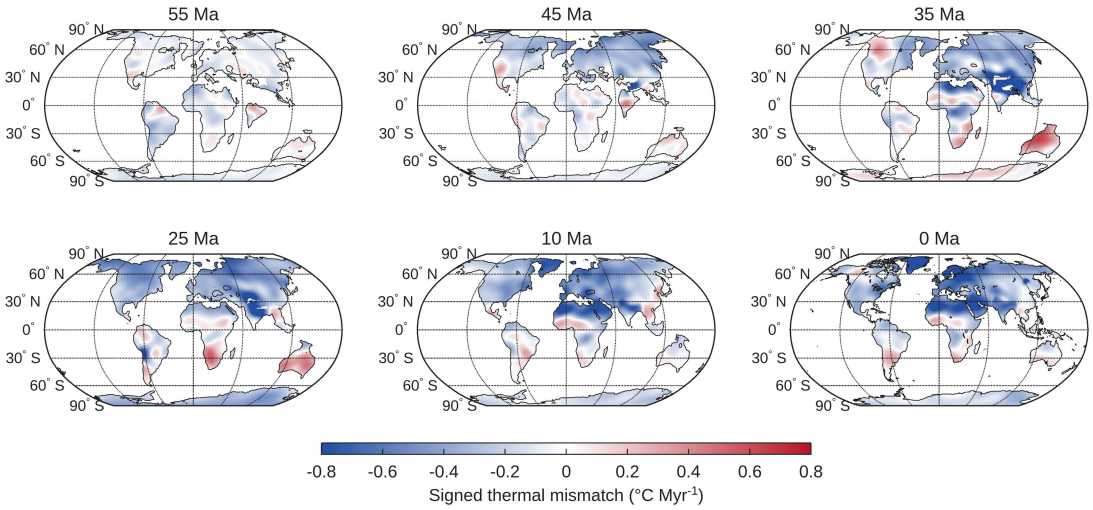


Fig. 1: **Signed thermal mismatch experienced along land trajectories.** Experienced temperature change in six representative 5 Myr intervals over the last 60 Myr. Colours show the rate of temperature change experienced by each land parcel as it moves with its plate (°C Myr^{-1}), which combines climate change in place with drift across spatial temperature gradients. Negative values indicate cooling; positive values indicate warming. A parcel can warm while global climate cools if it migrates equatorward fast enough, and can hold near-zero mismatch under strong climate change if its motion happens to track the shifting isotherms. Near-zero values identify land where the thermal regime persisted.

Combining these thermal mismatch trends with palaeovegetation biomass reconstructed using the model of Gurung et al. [32], we mapped interval stability gain, the stability accrued within each successive 5-Myr interval (**Fig. 2a–f**). Between 60 and 50 Ma, expansive biomes achieved peak stability gains, interspersed with localized instability. As global climate underwent major reorganization in the mid-Eocene, these spatial configurations shifted abruptly, imposing a severe macroevolutionary bottleneck on biotas trapped within expanding zones of low stability gain. By the late Cenozoic, intensifying aridification had depressed primary productivity across

the modern Saharan, Arabian, and major Southern Hemisphere deserts, establishing them as enduring geographic barriers of limited habitability.

We quantified the long-term environmental continuity experienced by present-day land parcels as cumulative stability (CS; **Box 1**). Because CS depends on how biota respond to environmental change, we sampled 100,000 combinations of plausible values for its five biological parameters (thermal and resource sensitivities, thermal niche breadth, resilience tolerance and biomass threshold) and report the ensemble mean (**Fig. 2g**). The resulting map shows a pronounced latitudinal gradient, with CS highest in the tropics, most notably in Amazonia, central Africa and parts of Australasia, and secondary maxima in western North America and East Asia. This latitudinal structure persists across the parameter ensemble (**Fig. 2h**).

Regions with CS > 20 Myr, which we define as macroevolutionary refugia (**Methods**), cover about 42.2 $\times 10^6$ km^2 of present-day land. To isolate the contribution of plate motion to this pattern, we evaluated thermal change at fixed coordinates within each time step, thereby removing the effect of continental drift. Compared with this counterfactual, plate motion reduces the area of refugia by about 5.4×10^6 km^2, roughly half the area of Europe (**Extended Data Fig. 2**).

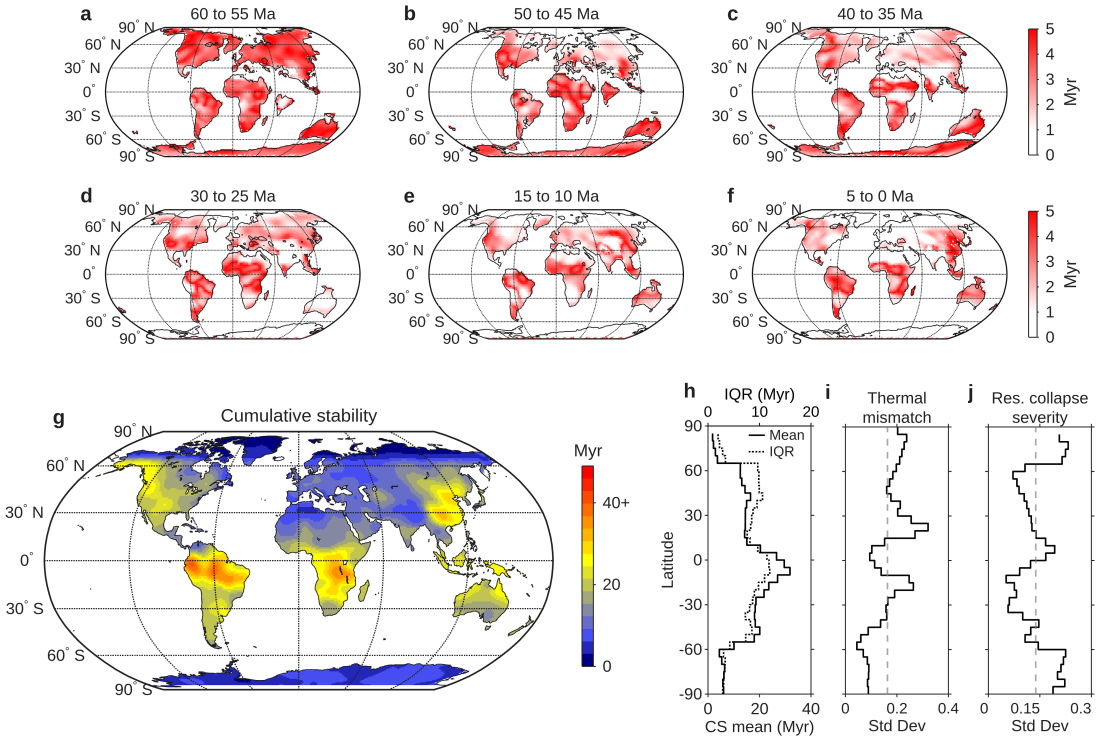


Fig. 2: **Cumulative stability, its uncertainty and environmental volatility over the last 60 million years. a–f,** Stability gained within six representative 5 Myr intervals, from 60–55 Ma (**a**) to 5–0 Ma (**f**), in Myr. Accumulation reflects the thermal stability experienced by each land parcel, weighted by the ecological capacity limit (**Box 1**). **g,** Present-day cumulative stability (CS) integrated from 60 Ma to the present (Myr), shown as the ensemble mean across 100,000 parameter combinations (**Box 1**; **Methods**). **h,** Latitudinal profile of mean CS and ensemble uncertainty, given as the interquartile range (IQR; 25$^{\text{th}}$–75$^{\text{th}}$ percentiles, Myr) across ensemble members, averaged within 5° latitudinal bands. **i,j,** Latitudinal profiles of environmental volatility over the past 60 Myr for experienced thermal change (°C Myr^{-1}; **i**), and resource collapse severity, $1 - R$ (dimensionless; **j**). Black lines show the standard deviation of each variable within 5° latitudinal bands; dashed vertical lines mark the mean of these band standard deviations.

To understand the latitudinal pattern of CS, we examined how experienced thermal change and resource collapse severity varied across palaeolatitudinal bands over the past 60 Myr (**Fig. 2i,j**). Variability in experienced thermal change was lowest near the equator and at southern high palaeolatitudes, and highest in two subtropical bands centred near 25°N and

15°S, with northern high latitudes moderately above the global mean (**Fig. 2i**). The equatorial minimum is consistent with the weak spatial temperature gradients of the tropics, which limit the thermal change produced by drift, whereas the subtropical maxima coincide with the palaeolatitudes traversed by India during its rapid northward drift. Resource collapse severity showed a different pattern, with the highest variability at both polar extremes and in a northern tropical band near 10–15°N, and the lowest in the southern subtropics (**Fig. 2j**). High-latitude resource volatility is consistent with Cenozoic cooling and vegetation loss (**Fig. 2a–f**), whereas low-latitude volatility is linked to Miocene–Pliocene aridification (ca. 10–2.5 Ma). Thus, the equatorial CS maximum reflects low thermal and moderate resource volatility, whereas low CS at high latitudes arises mainly from high thermal volatility and repeated resource collapse.

The effect of deep-time stability on modern biodiversity

CS integrates two constraints with distinct temporal structure (**Box 1**). Thermal continuity (CS_T), the time a parcel remains within its biota's thermal tolerance, only accumulates: once gained, it is never lost. Resource continuity (CS_R), the time a parcel sustains sufficient vegetation biomass, can instead be lost retroactively, as each resource collapse reduces its accumulated total (**Fig. 3a**). Comparing the two partitions the terrestrial surface into parcels limited by thermal continuity ($CS_T < CS_R$) and parcels limited by resource continuity ($CS_R < CS_T$). Resource-limited parcels concentrate in high-latitude and arid regions, where modelled vegetation biomass collapses are largest (**Fig. 3b**). Parcels retaining CS above 30 Myr are concentrated in tropical and equatorial regions, where both thermal stability and biomass density remain near their maxima throughout the the last 60 Myr (see **Supplementary Information** for reconstructions of temperature and vegetation biomass density across the full time series).

Empirical species richness [33–35] increases with CS in amphibians, reptiles, birds and mammals (**Fig. 3c,d**; **Extended Data Table 2**). In all four groups, the relationship accelerates where thermal continuity is the limiting component of CS. Where resource continuity is limiting, it accelerates in amphibians, reptiles and birds, and decelerates only in mammals, under both the bounded and the unbounded fit (**Extended Data Table 3**). Model selection with the Akaike information criterion (AIC) favoured bounded over unbounded models in five of eight group–regime combinations: all four groups under thermal limitation and reptiles under resource limitation (**Extended Data Table 2**). This preference, however, provides weak evidence for ecological ceilings on species richness. First, the bounded fits are constrained mainly by the accelerating part of the curve: no combination yielded a model that both decelerated and reached $\geq 90\%$ of its ceiling within the observed range of CS (10–45 Myr; **Extended Data Table 3**). Second, residual spatial autocorrelation reduces the effective sample size by more than two orders of magnitude. Once ΔAIC is adjusted accordingly, every comparison becomes statistically inconclusive ($|\Delta AIC_{eff}| \leq 0.6$). Third, when models are instead judged by their ability to predict withheld geographic regions, unbounded models are favoured in five of eight combinations. Bounded model win in amphibians and mammals under thermal limitation, where the fitted curves are still accelerating at 89% of their asymptotes, and in mammals under resource limitation, the only case in which the relationship decelerates; there, however, the bounded fit reaches only 75% of its asymptote within the data, and AIC favours the unbounded model ($\Delta AIC = +38.7$). Conversely, where a bounded model came closest to its ceiling (effectively 100% in reptiles under thermal limitation), the unbounded alternative predicted better (**Extended Data Table 2**). None of the eight combinations therefore indicates a ceiling. These patterns are largely insensitive to position along the generalist–specialist continuum (**Extended Data Fig. 3**).

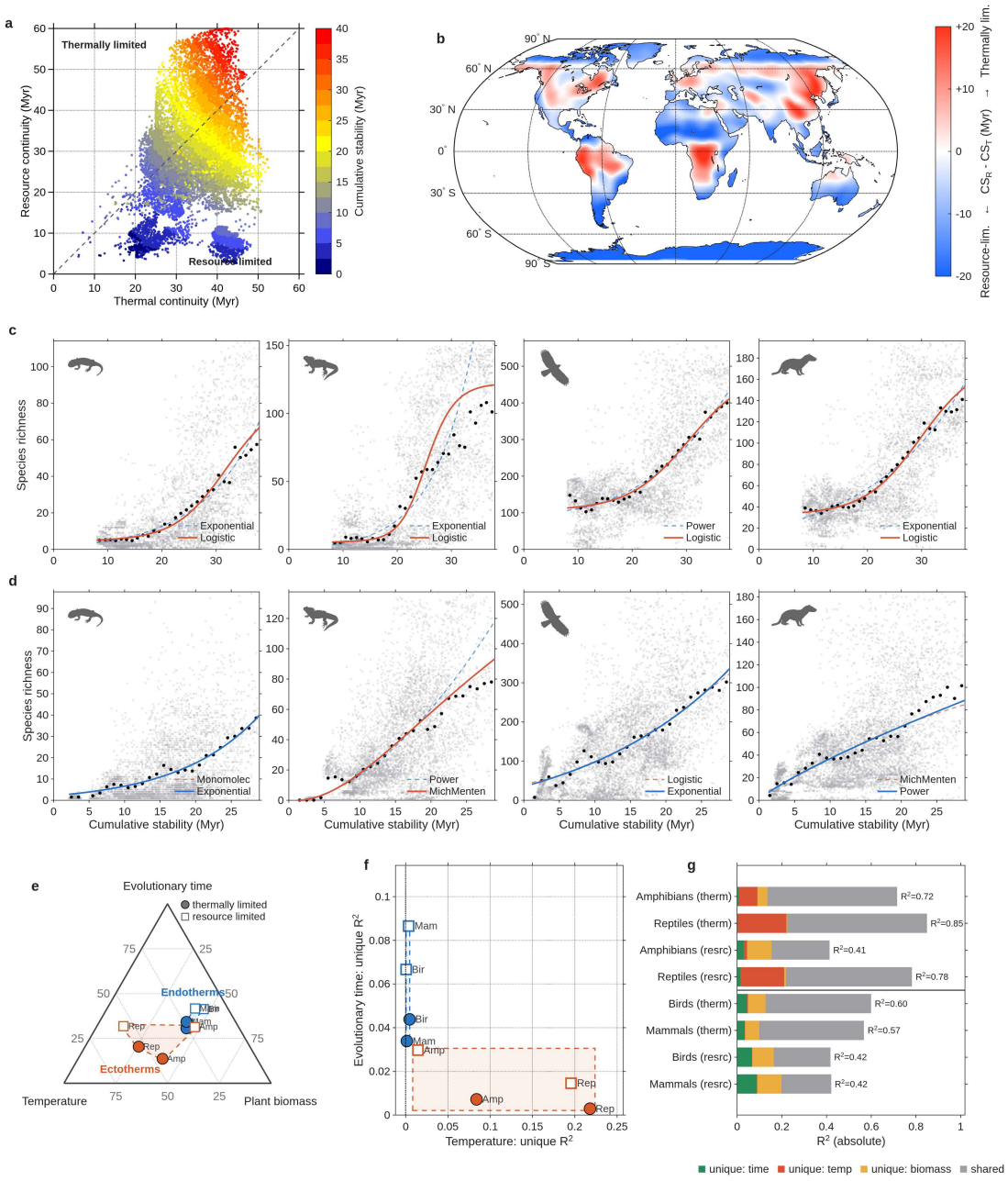


Fig. 3: **Cumulative environmental stability, its limiting constraints, and their relation to modern species richness. a**, Constraint space comparing thermal continuity (CS_T) and resource continuity (CS_R) for each habitat parcel, coloured by its cumulative stability (CS) in Myr. **b**, Global map of the difference between resource and thermal continuity ($CS_R - CS_T$, Myr), highlighting thermally limited (red) and resource-limited (blue) parcels. **c,d**, Marginal scaling of species richness against CS for four terrestrial vertebrate clades, in thermally limited parcels ($CS_T < CS_R$; **c**) and resource-limited parcels ($CS_R < CS_T$; **d**). Black dots are binned means; solid lines show the selected model (red, bounded; blue, unbounded), dashed lines display the rival family. **e**, Ternary plot of explained-variance composition among time, temperature and vegetation biomass, for endotherms (blue) and ectotherms (red). **f**, Uniquely attributable variance (absolute R^2) for time against temperature. **g**, Variance decomposition showing unique contributions of time (green), contemporary temperature (red) and vegetation biomass (yellow), with shared/confounded variance (grey), by clade and limitation regime.

Partitioning variance among CS (or time) and two contemporary variables, temperature and vegetation biomass, reveals a broad metabolic divide in the environmental correlates of species

richness (**Fig. 3e–g** and **Extended Data Table 4**). Endotherm richness is predominantly associated with time and biomass (74–88% of explained variance), whereas ectotherm richness is more closely tied to contemporary conditions (**Fig. 3e**). Temperature is the leading factor for reptiles in both regimes (54–55%), and temperature and biomass together account for 86% in amphibians under thermal limitation. Amphibians under resource limitation are the exception. Their partitioning resembles that of endotherms (time 31%, biomass 48%, temperature 21%). This divide is even clearer in uniquely attributable variance (**Fig. 3f**, **Extended Data Table 4**), although most explained variance is shared among predictors in every group–regime combination. Unique temperature effects are near-zero for endotherms, leaving time and biomass as their main unique contributors, whereas ectotherms rely primarily on contemporary conditions. Total explained variance drops under resource limitation for amphibians, birds and mammals ($R^2_{\text{tot}} = 0.41$–0.42, versus 0.57–0.72), but it remains high for reptiles (0.78–0.85) (**Fig. 3g**). Together, these results suggest that deep-time stability contributes more to modern species richness in endotherms, whereas contemporary climate is the stronger correlate of ectotherm richness, particularly in reptiles.

Nature conservation infrastructure fails to capture macroevolutionary refugia

Our analysis identifies the present-day land areas that have accumulated the most thermal and resource stability over the past 60 Myr (**Fig. 2g**). To determine whether current conservation frameworks safeguard these macroevolutionary refugia (CS > 20 Myr), we intersected the CS map with terrestrial protected areas from the World Database on Protected Areas (WDPA) and other effective area-based conservation measures (OECMs) [36]. We considered the full gradient of conservation strictness, from IUCN Categories I–VI to sites without a reported category ('Other/Unreported'). We classified CS independently within each of 100,000 simulations, so that the regional area estimates propagate species-response uncertainty into the reported interquartile ranges.

Globally, 77.9% of macroevolutionary refugia lie outside protected areas, leaving a median unprotected extent of 32.9 million km^2 (IQR: 16.0–53.1 million km^2; **Fig. 4**). Asia shows both the largest absolute gap and the most severe proportional deficit, with 91.5% of its stable regions unprotected (10.0 million km^2, IQR: 4.5–16.7), followed proportionally by North America at 87.8% (5.7 million km^2, IQR: 1.3–11.7). In absolute terms, Asia is followed by Africa (9.0 million km^2, IQR: 5.4–13.6), and by South America & the Caribbean (7.9 million km^2, IQR: 4.8–10.3). Africa and South America & the Caribbean nevertheless show the lowest proportional deficits (77.5% and 61.8%), indicating comparatively broader coverage. Europe, West Asia and the Polar region are absent from this comparison because they retain negligible land above the 20 Myr CS threshold.

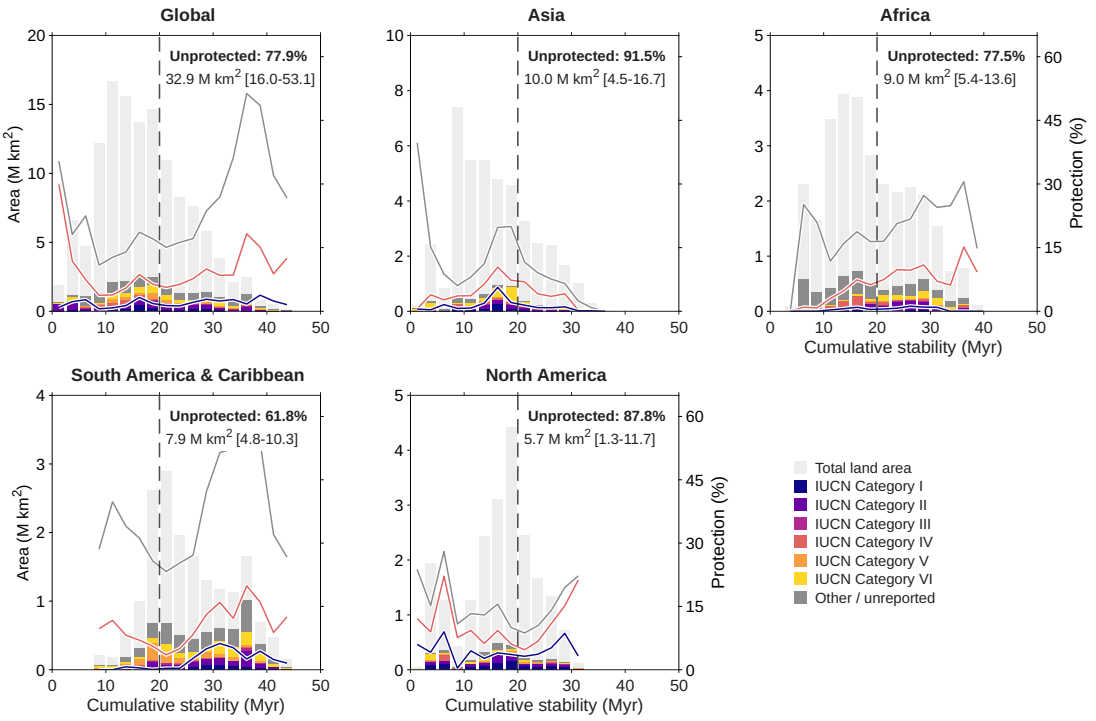


Fig. 4: **Cumulative stability and current protection coverage.** Global land and regions containing land above the cumulative stability (CS) threshold (CS > 20 Myr). Light grey bars show the distribution of land area across 2.5-Myr bins of CS (left axis, million km^2). Stacked bars show the protected area within each bin by IUCN management category. Lines (right axis) show the percentage of land in each bin protected under Category I alone (blue), Categories I–IV (orange) and all categories (grey). Annotations give the percentage and area of stable land outside any protected area, as medians across the simulation ensemble and the interquartile range (25$^{\text{th}}$–75$^{\text{th}}$ percentiles) of the area (in brackets). Full results are given in **Extended Data Tables 5–7**.

Protected areas cover 22.1% (IQR: 20.3–27.9%) of Earth's most stable environments, compared with 15.8% (IQR: 15.6–16.0%) of the remaining unstable land (**Fig. 5a**). The median per-simulation gap is 6.6 percentage points (pp; IQR: 5.0–12.2) and is positive in 95.6% of simulations. Decomposing coverage along the IUCN management gradient, however, shows that this advantage rests largely on the weakest protection categories. The gap is already present at the strictest tier (Category I; +0.6 pp) and across strict designations as a whole (Categories I–IV; +1.7 pp, IQR: 1.1–3.2; positive in 90% of simulations), but these account for only a quarter of the final gap. Within the strict tiers, National Parks (Category II) widen the gap by 1.7 pp, whereas Category IV narrows it by 0.7 pp, the only step that favours unstable land. The remaining three quarters come from the weakest designations (Categories V, VI and 'Other/Unreported'): Category VI adds 2.0 pp and 'Other/Unreported' areas a further 2.7 pp, the latter alone accounting for 41% of the final gap. Protection of stable environments thus depends disproportionately on weakly managed land. Strict nature reserves and wilderness areas (Category I) cover just 2.1% of these environments, whereas 'Other/Unreported' designations provide the largest single increase in coverage (7.7 pp). This reliance is more pronounced in Africa and in South America & the Caribbean, where Category VI and 'Other/Unreported' areas supply 58% and 62% of the protection of stable land, respectively (**Fig. 5a**).

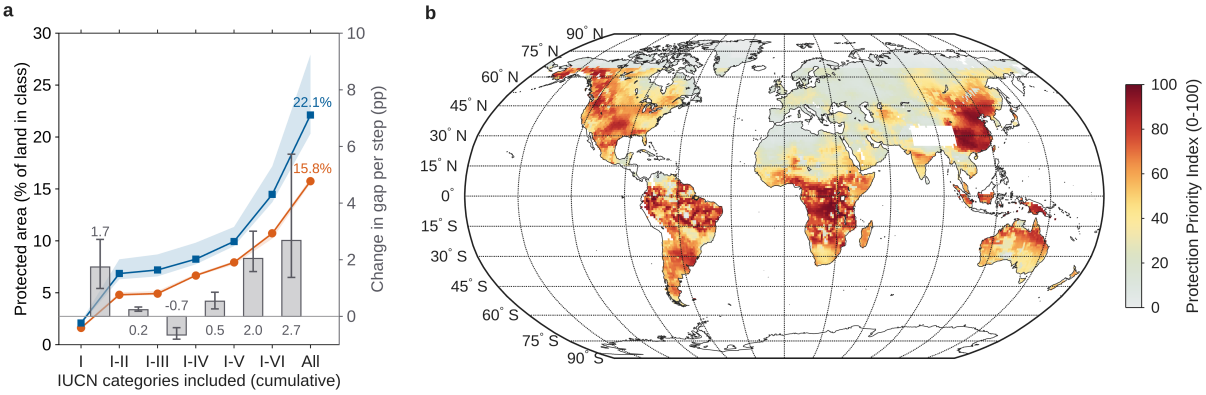


Fig. 5: **Protection of macroevolutionary refugia. a**, Cumulative protected area percentage across IUCN management categories (left axis) and the marginal change in coverage per step (right axis, grey bars). Blue squares, land with cumulative stability (CS) > 20 Myr (median 42.2 M km^2); orange circles, CS ≤20 Myr (86.3 M km^2). Lines show ensemble medians and shading the interquartile range (IQR) across 100,000 simulations, each carrying its own stability classification; values at the right give median coverage with all categories included. Grey bars (right axis), placed between successive category sets, show the change in the stable – unstable coverage gap as each category is added; error bars give the IQR and numbers the median change in percentage points. **b**, Global map of the Protection Priority Index (PPI), combining ensemble-mean CS with effectiveness-weighted protection coverage. High values (dark red) identify regions that combine high environmental stability with low effective protection. White land areas carry no PPI value: they either have no model cell or are excluded from the index (central Andes and Himalaya–Tibetan Plateau; see **Methods**).

To translate this conservation gap into a map, we combined CS with current protection into a protection priority index (PPI; **Fig. 5b**; see **Methods**). For each grid cell, the PPI is the product of a stability value, given by the percentile rank of the cell's CS among all land, and a protection shortfall, the fraction of the cell not effectively protected. Protection counts all WDPA areas, with less strict IUCN categories given lower weight to reflect weaker management. Because the two terms are multiplied, a cell scores highly only if it is both highly stable and poorly protected. The PPI therefore indicates where each additional square kilometre of protection would safeguard the most deep-time stability. The index is highest in eastern China, the Congo Basin and adjoining East and south-central Africa, Amazonia, much of the United States, Alaska and western Canada, and New Guinea and maritime Southeast Asia. Intermediate values extend across the West African forest belt, northern Australia and southern South America. The index is uniformly low across Europe, the Sahara, Arabia, and central and northern Asia, where there is little deep-time stability to protect. The ranking of regions by mean PPI was largely unchanged when we gave greater weight to stability or to the protection shortfall, counted only strictly managed protected areas, or weighted all protected areas equally (**Extended Data Table 8**).

Implications for understanding and conserving biodiversity

By quantifying the cumulative stability (CS) experienced by land parcels in tectonic transit, our Lagrangian framework changes both how present-day richness patterns should be interpreted and how their protection should be prioritised. First, terrestrial vertebrate diversity appears to be far from equilibrium. The absence of an asymptote in the species richness–CS relationship indicates that these groups have not reached ecological saturation, which helps reconcile the dispute over whether regional diversity is bounded [37–39]. Ecological limits may exist, but environmental continuity is rarely sustained long enough for biotas to reach them. Directional change, such as continental drift and long-term climatic shifts, alters the environmental conditions against which a diversity ceiling is defined. At finer time scales, Milankovitch-driven climatic oscillations, operating below our model's temporal resolution, disrupt evolutionary trajectories [15] and truncate incipient lineages before speciation is complete [40]. As a result, present-day richness is a historically contingent accumulation, not an equilibrium to which biotas return after disturbance. Because macroevolutionary refugia consist of lineages accumulated over

millions of years, rather than assemblages that rebuild rapidly through recolonisation or recent diversification, their loss would be irreversible on any timescale relevant to human societies [41].

Second, no single explanation of richness gradients holds across vertebrates. Deep-time stability and biomass explain most of the unique variance in endotherm richness, whereas contemporary climate dominates in ectotherms, consistent with physiological predictions [14, 42]. Because endotherms evolve thermal niches faster and maintain wider latitudinal ranges [43], their richness integrates the full environmental history of a land parcel. Ectotherms, by contrast, are thermally conservative; contemporary climate closely approximates the conditions their surviving lineages have experienced, leaving little independent signal on the deep-time historical axis. The two groups are therefore exposed to different components of global change. Ectotherm diversity responds most directly to shifts in contemporary climate, while endotherm diversity depends more on long-term environmental stability and resource availability. In light of these results, regions that combine present-day climatic buffering with deep-time stability represent the strongest candidates for safeguarding both groups.

Finally, our analysis shows that current protected area networks leave most macroevolutionary refugia unprotected. This gap leaves a disproportionate share of Earth's phylogenetic heritage exposed to ongoing land-use change [44]. As countries work towards Target 3 of the Kunming–Montreal Global Biodiversity Framework, which calls for protecting at least 30% of land and inland waters by 2030 [45], where that 30% is placed will matter as much as how much is protected. Our analysis offers one axis along which sites of irreplaceable evolutionary value can be identified. Safeguarding these regions, however, requires more than static boundaries. Treating fixed conservation networks as permanent biodiversity repositories overlooks the dynamic reality of a rapidly warming planet [6, 7]. Where a bioclimatic envelope exits a protected area faster than resident species can migrate or adapt, reserves risk functioning as climatic traps rather than refugia [28, 46]. Species in such reserves may persist long after the conditions that sustained them have moved on, accumulating a kinematic debt. As with extinction debt [31, 47], this lag is both a hazard, because the losses it implies are invisible to assessments based on current occurrence, and an opportunity, because they can still be averted. Averting these losses requires evaluating habitat connectivity not only as a spatial landscape property but also in relation to shifting climate and productivity gradients [48, 49].

Caveats and future directions

Our predictions rest on three simplifications, each of which defines a route for extending the framework. First, the palaeoenvironmental fields derive from a single climate–vegetation simulation, and therefore the reported uncertainty captures variability within that model rather than structural differences between models. Because the framework accepts any gridded palaeoclimate reconstruction as input, applying it across a multi-model ensemble would allow this structural uncertainty to be quantified. Second, relative plate motions and palaeolatitudes are well constrained for the Cenozoic, but palaeolongitudes are less so, and this uncertainty could affect the advective term $\mathbf{v}_{\mathrm{tec}} \cdot \nabla T$ where east–west temperature gradients are strong. Incorporating emerging probabilistic plate reconstructions that explicitly represent palaeolongitudinal uncertainty would allow this to be propagated through the framework. Third, topography is prescribed rather than dynamically evolved, so mountain building, erosion and drainage reorganisation, which help shape the spatio-temporal evolution of biodiversity [50], are not yet explicitly resolved; coupling with landscape evolution models [51] would capture these processes.

The protection priority index is therefore best viewed as a hypothesis rather than a final ranking. Because the proposed framework is agnostic to its inputs, multi-model palaeoclimate ensembles, probabilistic plate reconstructions and landscape evolution models can each be readily incorporated, allowing protection priority to be defined not by any single reconstruction but by agreement among independent realisations of Earth's history. More broadly, this approach shifts conservation planning from mapping where biodiversity is today towards identifying where the deep-time processes that generated it are recorded. Such knowledge is essential for anticipating how ongoing environmental change may disrupt the processes that have shaped biodiversity over millions of years.

Methods

Palaeogeographic model

The palaeogeographic model underlying this study is an updated version of that described in ref. [27]. The base reconstruction model is that of Merdith et al. [24] (GPlates files v1.1; https://doi.org/10.5281/zenodo.13635864), defined in a palaeomagnetic reference frame. This frame places continents relative to Earth's spin axis, so reconstructed palaeolatitudes are consistent with the latitudinal structure of climate simulated by Earth system models. From this reconstruction, we generated maps of palaeotopography and palaeobathymetry at $0.5° \times 0.5°$ resolution. Palaeotopography and shallow-marine bathymetry were taken from the PALEOMAP reconstructions of Scotese and Wright [52], available at 5-Myr intervals. Because the two reconstructions place the continents in slightly different positions, we shifted the PALEOMAP topography onto the plate configuration of ref. [24], following the procedure of ref. [27].

Palaeoenvironmental reconstructions

We reconstructed palaeoenvironmental conditions using the spatially resolved global climate-biogeochemical model SCION (version 1.3) [53], utilizing updated palaeogeographic maps defined at 5-million-year intervals (see **Supplementary Information**) To drive the surface processes within SCION, we updated its climate emulator using a large, newly generated lookup table of 1,090 climate simulations conducted with the Fast Ocean Atmosphere Model (FOAM v1.5). Our FOAM setup consists in an atmospheric model coupled to a 50-meter mixed-layer "slab" ocean and a thermodynamic sea-ice model. This gridded ensemble spans 109 time slices (540 to 0 Ma) and 10 atmospheric CO_2 concentrations (0.25 to 128 times pre-industrial levels), providing a comprehensive matrix of climatic responses to continuous continental shifts and varying greenhouse gas forcing.

To capture the terrestrial biosphere's active role in deep-time climate, SCION was dynamically coupled with the FLORA vegetation model [32]. Based on the LPJ dynamic global vegetation model [54], FLORA utilizes regional environmental outputs from SCION (e.g. surface temperature, runoff, insolation, and atmospheric CO_2 and O_2) to calculate spatially resolved terrestrial photosynthesis and carbon allocation. These regional vegetation metrics are recalculated at every model time step and feedback directly into SCION to inform land-derived organic carbon burial and continental weathering rates. This bidirectional coupling creates a self-consistent global loop where vegetation biogeography directly regulates the long-term C-O-P-N-S cycles.

Because standard forward-model outputs did not perfectly align with proxy-derived Cenozoic global temperature records, we applied a targeted model inversion approach to construct an accurate, proxy-matched baseline for the Cenozoic. We modified the global rate of tectonic CO_2 degassing, implementing a 35% reduction over the era to reproduce the broad-timescale cooling trend. Baseline degassing rates were also adjusted to account for FOAM's inherently lower preindustrial global average temperature (13 °C versus the 14 °C proxy consensus). This inversion yields modelled Cenozoic CO_2 levels slightly above proxy estimates, arising in part from FOAM's relatively low climatic sensitivity, which falls right between the multimodel mean values calculated by Zelinka et al. (2020) [55] for the CMIP5 and CMIP6 ensembles, but contrasts with higher-end members featured in these ensembles such as CESM2. In the model, the resulting CO_2 fertilization of plants is counteracted by correspondingly elevated atmospheric O_2, which limits vegetation through photorespiration and wildfires. This dynamic ensures our global biomass predictions remain robust and self-consistent. The final modelled outputs for surface air temperature and terrestrial biomass were subsequently mapped onto a high-resolution grid using linear interpolation.

Comprehensive details regarding model setup, boundary conditions, orbital configurations, and comparisons against proxy records are provided in the Supplementary Information, (**Supplementary Methods** and **Figs. S1**–**S5**).

Climate velocity

To quantify the geographic speed and direction required for a species to maintain its thermal niche over time, we calculated climate velocity ($\mathbf{v}_{\text{clim}}$) following Loarie et al. [6], using global

temperature fields derived from SCION model simulations. Because our simulated parcels represent moving tectonic plates over geological time, we adopted a framework that isolates the local geographic climate signal from tectonic advection.

To address numerical instability in climatically uniform regions and mitigate coordinate distortion at the poles, we implemented a 3D-projected neighbourhood tracking algorithm. Palaeo-coordinates were projected into a 3D Cartesian system using Earth's radius ($R = 6371$ km):

$$X = R\cos(\theta_{\text{lat}})\cos(\phi_{\text{lon}}) \qquad Y = R\cos(\theta_{\text{lat}})\sin(\phi_{\text{lon}}) \qquad Z = R\sin(\theta_{\text{lat}}) \tag{1}$$

For each parcel, we identified its 20 nearest neighbours in this Cartesian frame.

To calculate the spatial gradient ($\boldsymbol{\nabla} T = [g_{\text{lon}}, g_{\text{lat}}]$) and the local Eulerian temporal tendency ($\partial T/\partial t$), we solved local least-squares regressions. For the spatial gradient at time t, we calculated the relative spatial displacement ($\Delta x, \Delta y$) of the valid neighbourhood points. To prevent artefacts across the anti-meridian, longitudinal differences were wrapped to the interval $[-180°, 180°]$ before conversion to distance ($\Delta x = R\cos\theta_{\text{lat}}\,\Delta\phi_{\text{lon}}$, $\Delta y = R\,\Delta\theta_{\text{lat}}$, angles in radians). To suppress baseline noise, neighbours closer than 100 km were excluded from the spatial gradient fit, and the fit was attempted only where at least three valid neighbours remained beyond that separation. Note that the plane fits used for local temperature estimates retained the full 20-neighbour set.

We then fitted the local plane:

$$\Delta T \approx c_0 + g_{\text{lon}}\Delta x + g_{\text{lat}}\Delta y \tag{2}$$

where c_0 is a fitted intercept absorbing any local offset. This was solved via QR decomposition ($\mathbf{A} \setminus \Delta\mathbf{T}$), which provides better numerical conditioning than the normal-equations form. Fits returning implausible slopes ($|\boldsymbol{\nabla} T| \geq 5\,°\text{C}\,\text{km}^{-1}$) were rejected. Where no stable fit could be obtained, the gradient was left undefined and the parcel excluded from velocity calculations for that specific interval.

The Eulerian temporal tendency was obtained by fitting an equivalent local plane to the $t+1$ temperature field. Crucially, this was anchored to the parcel's geographic position at time t by finding the $t+1$ neighbours nearest to the parcel's past location, thereby factoring out the parcel's tectonic displacement. The temporal tendency was calculated by differencing this intercept against the plane-fitted temperature at t:

$$\frac{\partial T}{\partial t} \approx \frac{\hat{T}_{t+1}(\mathbf{x}_t) - \hat{T}_t(\mathbf{x}_t)}{\Delta t} \tag{3}$$

We computed climate velocity as the local rate of temperature change divided by the spatial temperature gradient [6], adopting the vector form of Burrows et al. [7]. Because this ratio diverges where the climate surface is flat, we imposed a minimum spatial gradient $g_{\text{min}} = 0.0015\,°\text{C}\,\text{km}^{-1}$ to set the speed, while preserving the direction of the unfloored gradient:

$$\mathbf{v}_{\text{clim}} = -\frac{\partial T/\partial t}{\max(|\boldsymbol{\nabla} T|,\, g_{\text{min}})}\left(\frac{\boldsymbol{\nabla} T}{\max(|\boldsymbol{\nabla} T|,\, \epsilon)}\right) \tag{4}$$

Here, $\partial T/\partial t$ is in $°\text{C}\,\text{Myr}^{-1}$, $|\boldsymbol{\nabla} T|$ is in $°\text{C}\,\text{km}^{-1}$, so $\mathbf{v}_{\text{clim}}$ is in $\text{km}\,\text{Myr}^{-1}$, and $\epsilon = 10^{-6}$ prevents division by zero in the direction vector. When $|\boldsymbol{\nabla} T| \geq g_{\text{min}}$, this formulation satisfies the isotherm-displacement condition $\partial T/\partial t + \mathbf{v}_{\text{clim}} \cdot \boldsymbol{\nabla} T = 0$; otherwise, the speed is capped to provide a bounded estimate of isotherm displacement. The full time series of global climate velocity maps is displayed in Supplementary Information (**Fig. S6**).

Tectonic velocity

Tectonic velocity was calculated by tracking the Lagrangian displacement of coordinate parcels between consecutive time slices (t and $t+1$). To correct for boundary artefacts when tracking parcels across the anti-meridian (dateline), a modulo transformation was applied to the longitudinal delta. The latitudinal and longitudinal components of the tectonic velocity vector were computed in physical space (km/Myr), correcting the longitudinal distance for spherical

geometry at the midpoint latitude of the interval, $\bar{\theta} = (\theta_t + \theta_{t+1})/2$, rather than at its start, since a parcel may traverse several degrees of latitude within a single 5-Myr step:

$$v_{\text{tec,lat}} = \frac{c\,(\theta_{t+1} - \theta_t)}{\Delta t} \tag{5}$$

$$v_{\text{tec,lon}} = \frac{c\,[((\phi_{t+1} - \phi_t + 180) \bmod 360) - 180]\cos(\bar{\theta})}{\Delta t} \tag{6}$$

where θ represents latitude, ϕ represents longitude in degrees, $c = \pi R/180 \approx 111.19$ km deg^{-1} is the physical distance conversion factor per degree (with $R = 6371$ km), and Δt is the 5-Myr time step. The full time series of global tectonic velocity maps is displayed in Supplementary Information (**Fig. S7**).

Kinematic offset and thermal mismatch

To quantify the true physiological stress exerted on sedentary lineages, we decoupled absolute climate velocity from tectonic velocity. From a macroevolutionary perspective, climate velocity ($\mathbf{v}_{\text{clim}}$) overestimates the dispersal requirements if the tectonic plate is drifting in the same direction as the shifting climate, and underestimates it if the plate is drifting in the opposite direction. We first calculated the kinematic offset ($\Delta\mathbf{v}$) as the vector difference between climate and tectonic velocities:

$$\Delta\mathbf{v} = \mathbf{v}_{\text{clim}} - \mathbf{v}_{\text{tec}} \tag{7}$$

This vector difference conceptually drives the thermal mismatch (M_{thermal}) experienced by a lineage. In an Eulerian framework, thermal mismatch is approximated by adding the local temporal tendency to the advection of the parcel across the spatial temperature gradient ($\frac{\partial T}{\partial t} + \mathbf{v}_{\text{tec}} \cdot \boldsymbol{\nabla} T$). We instead calculated M_{thermal} directly as the absolute material derivative ($\frac{DT}{Dt}$) along each land parcel's tectonic trajectory:

$$M_{\text{thermal}} = \left|\frac{DT}{Dt}\right| = \left|\frac{T(t+1) - T(t)}{\Delta t}\right| \tag{8}$$

By taking the first difference of temperature for the identical material point across consecutive time slices, this approach intrinsically captures both the geographic drift across climatic gradients and the global temporal shift in climate. Because it follows the exact Lagrangian trajectory, it requires no neighbourhood search, no spatial gradient estimation, and no velocity ceiling. The full time series of vector difference maps and the signed thermal mismatch are displayed in **Extended Data Fig. 1** and **Fig. S8**.

Cumulative stability

We calculated the uninterrupted environmental persistence of modern landscapes as cumulative stability (CS), a Lagrangian metric that integrates the duration of thermal and resource continuity experienced by a parcel of land in tectonic transit. This metric is evaluated dynamically at discrete time steps and is governed by two primary constraints: instantaneous thermal stability and a resource retention factor.

Instantaneous thermal stability ($S_i(t)$) quantifies the thermal mismatch generated by the divergence of tectonic and climate velocities over a given time step (Δt). We modelled this stability as an exponential decay function:

$$S_i(t) = \exp\left(-k_T \frac{|\Delta T_i(t)|}{\Delta T_{\text{breadth}}}\right) \tag{9}$$

where $|\Delta T_i(t)|$ is the absolute temperature change experienced by the moving parcel i, $\Delta T_{\text{breadth}}$ is a representative thermal niche breadth (representing a generalised macroscopic tolerance limit), and k_T is the thermal sensitivity constant. $S_i(t)$ therefore decays exponentially with the ratio of $|\Delta T_i(t)|$ to $\Delta T_{\text{breadth}}$, at a rate modulated by k_T. $S_i(t) = 1$ when the parcel experiences no thermal change, and higher values of k_T produce a steeper loss of stability for a given thermal mismatch.

While instantaneous thermal stability tracks continuous climatic stress, accumulated stability can also be lost abruptly through resource collapse. To model this, we defined a resource retention factor, $R_i(t)$, which sets the fraction of previously accumulated stability carried forward across a time step. $R_i(t)$ depends on the relative decline in vegetation biomass (B) along each parcel's trajectory between consecutive time steps:

$$\delta_i(t) = -\frac{B_i(t) - B_i(t - \Delta t)}{B_i(t - \Delta t)} \tag{10}$$

Normalising by prior biomass ($B_i(t - \Delta t)$) means that retention reflects the relative severity of collapse experienced by the local ecosystem rather than its absolute magnitude. To represent the buffering capacity of ecosystems, declines smaller than a resilience tolerance, ρ, are ignored, and the retention factor decays exponentially with the part of the decline exceeding it:

$$R_i(t) = \exp\left(-k_R \max\left(0,\ \delta_i(t) - \rho\right)\right) \tag{11}$$

where k_R is a resource sensitivity constant. When biomass is stable (i.e., increases or declines by less than ρ), $R_i(t) = 1$ and accumulated stability is fully retained. Larger declines discount it exponentially at a rate modulated by k_R.

To evaluate the immediate environmental stress experienced by a tracked parcel at any specific geological time slice, we calculated the interval stability gain ($\mathrm{IS}_i(t)$), defined as the thermal stability ($S_i(t)$) realised over the interval, weighted by the ecological capacity of the parcel:

$$\mathrm{IS}_i(t) = S_i(t)\, P_i(t)\, \Delta t, \qquad P_i(t) = \max\left[0.01,\ \min\left(1,\ \frac{B_i(t)}{B_{\mathrm{thresh}}}\right)\right] \tag{12}$$

where $P_i(t)$ is a productivity weight and $B_{\mathrm{thresh}} = \beta\, B_{95}$ is a viability threshold, defined as a fraction β of the 95$^{\mathrm{th}}$ percentile of vegetation biomass across all parcels and time steps. Parcels with biomass at or above B_{thresh} realise their full thermal stability ($P_i = 1$), whereas stability gains in less productive parcels are scaled down in proportion to their biomass. $\mathrm{IS}_i(t)$ quantifies the stability gain realised by the parcel over each 5-Myr interval and therefore ranges from 0 to 5 Myr.

Finally, we calculated the cumulative stability of each parcel (CS_i) recursively along its palaeogeographic trajectory, from 60 Ma ($\mathrm{CS}_i = 0$) to the present. CS_i quantifies the thermal stability accumulated by a parcel, discounted by its history of resource collapse. Rather than a simple time integration, at each time step the prior accumulation is multiplied by the resource retention factor before the new interval stability gain is added:

$$\mathrm{CS}_i(t) = \mathrm{CS}_i(t - \Delta t), R_i(t) + \mathrm{IS}_i(t) \tag{13}$$

where $R_i(t)$ is the resource retention factor and $\mathrm{IS}_i(t)$ is the interval stability gain. Because $R_i(t)$ multiplies the entire accumulated stock rather than the current increment, a severe resource collapse proportionally discounts a parcel's full prior history. Conversely, because the thermal stability, productivity weight and retention factor are all bounded by 1, a parcel can gain at most 5 Myr of stability per 5-Myr interval, so stability cannot accumulate faster than elapsed time and CS_i ranges from 0 to 60 Myr.

Macroevolutionary refugia

We define macroevolutionary refugia as present-day land with CS > 20 Myr. The area-weighted distribution of ensemble-mean CS shows no clear bimodality (**Fig. S9**), so no natural break separates refugia from other land. We therefore evaluated the refugium threshold (θ) against two independent references. First, six partition criteria applied to that distribution place the break between 16.9 and 23.4 Myr: the median (16.9 Myr); two-class Jenks natural breaks, which minimise within-class variance and for two classes coincide with Otsu's method (19.1 Myr) [56, 57]; the midpoint of the robust, percentile-trimmed range (19.7 Myr); the upper tercile (20.7 Myr); the midpoint of the full observed range (22.9 Myr); and the upper quartile (23.4 Myr). A two-component Gaussian mixture (16.8 Myr) is also shown for reference. Second, 20 Myr is one-third of the maximum stability attainable in the model (60 Myr, i.e. twelve 5-Myr intervals

from 60 to 0 Ma). At this threshold, refugia occupy about 33% of land, and roughly half of that area remains a refugium in at least 75% of simulations ($P_{25} > \theta$). Raising the threshold increasingly restricts refugia to thermally limited land, from 66% at 20 Myr to 95% at 30 Myr (**Fig. S10**), and refugia defined at higher thresholds are nested subsets of those defined at lower ones (**Figs. S11-S12**).

Sensitivity analyses

We ran 100,000 coupled simulations as a full factorial design, sampling ten levels of each of the five model parameters across ecologically plausible ranges to capture the physiological and trophic tolerances of terrestrial biota. The thermal niche breadth ($\Delta T_{\text{breadth}} \in [2, 10]^{\circ}$C) reflects the spectrum of fundamental thermal niches, from specialised taxa with narrow thermal envelopes to adaptable generalists. The thermal and resource sensitivity constants ($k_T \in [1, 6]$; $k_R \in [1, 3]$) set the steepness of stability decay in S_i and R_i, respectively. The biomass threshold fraction ($\beta \in [0.15, 0.23]$, such that $B_{\text{thresh}} = \beta\, B_{95}$) and the resilience tolerance ($\rho \in [0, 0.1]$) account for differing baseline energy requirements and ecosystem buffering capacity. All parameters were sampled at evenly spaced levels, except k_R, which was sampled at log-spaced levels.

To ensure that the ensemble reflects plausible biological uncertainty rather than mathematically degenerate extremes, we evaluated all parameter ranges with a series of diagnostic tests before running the simulations. Because β is the only parameter with a direct external referent, its upper bound was calibrated against modern observations of terrestrial productivity [58], so that no more than 60% of the modern, non-glaciated land surface was classified as productivity-limited ($P_i < 1$). Because k_R and ρ act multiplicatively on accumulated stability, their limits were evaluated through their compounding effect over time: the upper bound of k_R was constrained so that the median parcel retained at least 5% of its accumulated stability over the full record, preventing a global collapse towards zero that would erase regional variance. Similarly, the bounds of k_T and $\Delta T_{\text{breadth}}$ were restricted so that S_i did not fall to near zero in more than 20% of parcel-steps. Finally, we checked the level spacing within the parameter grid to avoid skewing the ensemble mean and interquartile range, ensuring that the effect ratio between adjacent levels of k_R, the most sensitive parameter, did not exceed a factor of 4. This approach ensures that the identified macroevolutionary refugia are robust across varying degrees of ecological specialisation and vulnerability.

For each parcel, we calculated the mean, median and interquartile range (IQR) of CS_i across the 100,000 simulations. The mean across simulations is the value mapped and used for refugia classification. Zonal profiles of the mean and IQR were obtained by averaging parcel values within 1° latitudinal bins, which were aggregated into 5° bands for illustration purposes. To examine the drivers of CS_i, we additionally computed, for every parcel and time step, the resource collapse severity ($1 - R_i$), using the mean of each sampled parameter range. The variability of thermal mismatch ($|\Delta T_i|/\Delta t$) and of resource collapse severity was then summarised as the standard deviation within 5° latitudinal bands, pooling all time steps.

Species richness data acquisition

Global species richness data for amphibians, reptiles, birds and mammals were obtained as 10-km resolution rasters in the World Eckert IV equal-area projection from BiodiversityMapping.org [33]. For amphibians, birds and mammals, these rasters are derived from species range polygons compiled by the IUCN Red List of Threatened Species [59] and BirdLife International; for reptiles, they are derived from the range maps of the Global Assessment of Reptile Distributions (GARD) [34]. We used the December 2017 release for amphibians, the March 2018 release for mammals and version 7 for birds. The bird richness data are restricted to breeding ranges and exclude seabirds, so that they reflect terrestrial patterns. Before resampling, pixels carrying each raster's nodata value (255 for the 8-bit amphibian and mammal rasters; 65,535 for the 16-bit reptile and bird rasters) were excluded.

The richness rasters are defined in projected Eckert IV coordinates (ESRI:54012), whereas the climate and stability data are defined in geographic coordinates. We therefore wrapped longitudes to $[-180^{\circ}, 180^{\circ}]$, projected the geographic coordinates forward into Eckert IV metres, converted them to raster pixel positions, and assigned each location the value of the nearest raster cell (nearest-neighbour sampling). This was done both at the land data points used in

the statistical analyses and on the regular longitude–latitude grid used for mapping, where grid cells without a stability estimate were masked.

Model selection

To quantify the relationship between species richness and CS under different environmental limitations, we first divided land parcels into thermally limited and resource-limited regimes. Thermal cumulative stability (CS_T) accumulates instantaneous thermal stability, $S_i(t)$, along each parcel's trajectory,

$$\mathrm{CS}_{T,i}(t) = \mathrm{CS}_{T,i}(t - \Delta t) + S_i(t)\,\Delta t, \tag{14}$$

whereas resource continuity (CS_R) accumulates biomass-limited capacity and discounts the accumulated stock at each collapse,

$$\mathrm{CS}_{R,i}(t) = \mathrm{CS}_{R,i}(t - \Delta t)\,R_i(t) + \min\left(1, \frac{B_i(t)}{B_{\mathrm{thresh}}}\right)\Delta t, \tag{15}$$

where $R_i(t)$ is the resource retention factor and B_{thresh} is the ecological capacity threshold (**Methods**, section Cumulative stability). Both CS_T and CS_R were initialised at zero and, like CS, averaged across the 100,000 simulations. Their difference defines the limitation metric, $\Delta_i = \mathrm{CS}_{R,i} - \mathrm{CS}_{T,i}$: parcels with $\Delta_i > 0$ are thermally limited and those with $\Delta_i < 0$ are resource limited.

We excluded two regions where topography prevents palaeo-reconstructions from being reliably assigned to the locations they represent: the Andes (68 parcels; 0.47% of the data) and the Himalayas–Tibetan Plateau (207 parcels; 1.42%). Our plate-tectonic model operates on a two-dimensional surface and does not represent relief, so it inherently overestimates stability in active subduction zones such as the Andes and underestimates it in continent-to-continent collision zones such as the Himalayas.

We evaluated CS–richness relationships with two formulations. Marginal models describe how richness scales with CS without conditioning on contemporary environment:

$$h(Y) = \beta_0 + \beta_1\,\phi(\mathrm{CS};\boldsymbol{\psi}) + \varepsilon. \tag{16}$$

Partial models estimate the effect of CS conditional on modern mean annual temperature (T_z) and vegetation biomass density (B_z), both z-scored with global means and standard deviations:

$$h(Y) = \beta_0 + \beta_1 T_z + \beta_2 B_z + \beta_3\,\phi(\mathrm{CS};\boldsymbol{\psi}) + \varepsilon. \tag{17}$$

In both, Y is species richness and $h(Y)$ is either Y (additive error) or $\ln(Y+1)$ (multiplicative error); $\varepsilon \sim \mathcal{N}(0,\sigma^2)$ is the residual error; and $\phi(\mathrm{CS};\boldsymbol{\psi})$ is a function of untransformed CS (Myr) with shape parameters $\boldsymbol{\psi}$ (k, p, r, K_m or CS_0, depending on the form). For any fixed $\boldsymbol{\psi}$, ϕ evaluated at each parcel's CS is a known covariate, so the β coefficients follow from ordinary least squares; $\boldsymbol{\psi}$ was chosen to minimise the residual sum of squares over a grid and, for one-parameter forms, refined by golden-section search. Analyses were run separately for each clade and regime, after removing parcels in 1-Myr CS bins containing fewer than 25 parcels; clade–regime combinations with fewer than 200 parcels were not analysed.

Candidate forms of ϕ represent two macroevolutionary hypotheses. Unbounded (non-equilibrium) models assume no ceiling to species accumulation [37, 39]: on the identity scale, $\phi = \mathrm{CS}$ (linear), $e^{k\mathrm{CS}}$ (exponential) and CS^p (power); on the log scale, $\phi = \mathrm{CS}$ (exponential) and $\ln(\mathrm{CS}+c)$ (power). Bounded (equilibrium) models assume diversification slows as a carrying capacity is approached [60]: $\phi = 1-e^{-r\mathrm{CS}}$ (monomolecular), $\mathrm{CS}/(K_m+\mathrm{CS})$ (Michaelis–Menten) and $1/\{1+e^{-r(\mathrm{CS}-\mathrm{CS}_0)}\}$ (logistic), each fitted on both scales. Null models without a CS term were included as a reference.

AIC was computed from the Gaussian log-likelihood, counting the profiled parameters $\boldsymbol{\psi}$ as estimated parameters. Because likelihoods are not comparable across response transformations without accounting for the change of variables [61], log-scale models received a Jacobian correction,

$$\mathrm{AIC}_{\mathrm{corr}} = \mathrm{AIC}_{\log} + 2\sum_{i=1}^{n}\ln(Y_i+1), \tag{18}$$

placing all models on the likelihood scale of Y. For each clade and regime, we identified the best unbounded and best bounded model and quantified the evidence as $\Delta\mathrm{AIC} = \mathrm{AIC}_{\mathrm{bounded}} - \mathrm{AIC}_{\mathrm{unbounded}}$, with positive values favouring unbounded accumulation. To account for spatial autocorrelation, we deflated ΔAIC by $\lambda = n_{\mathrm{eff}}/n$, with the effective sample size n_{eff} estimated from the residuals of the best unbounded model by permutation, and compared predictive performance by spatial block cross-validation (10° blocks, 10 folds). Finally, we applied a saturation diagnostic to the best bounded model: a bounded fit was taken as evidence of a ceiling only if it reached more than 90% of its asymptote within the observed range of CS and its shape was decelerating.

Spatial correction for autocorrelation

Macroecological data are inherently spatially autocorrelated. Because AIC differences scale with the number of independent observations, autocorrelated residuals inflate ΔAIC and make model selection overconfident [62, 63]. We therefore deflated all AIC differences by an estimate of the effective sample size. For the best-fitting unbounded marginal model in each taxon × regime subset of n parcels, we computed Moran's I on the model residuals and estimated the range of residual autocorrelation, from which we derived an effective sample size n_{eff} following Clifford et al. [64]. The significance of residual autocorrelation was assessed against 199 random permutations of the residuals across parcel locations. This yields a deflation factor $\lambda = n_{\mathrm{eff}}/n \in (0, 1]$, and we report

$$\Delta\mathrm{AIC}_{\mathrm{eff}} = \lambda\,\Delta\mathrm{AIC} \tag{19}$$

where $\Delta\mathrm{AIC} = \mathrm{AIC}_{\mathrm{bounded}} - \mathrm{AIC}_{\mathrm{unbounded}}$ as defined above, so that positive values favour unbounded scaling. This rescales the evidence to that expected from n_{eff} spatially independent observations, shrinking apparent support that arises from autocorrelated residuals. We treated $\Delta\mathrm{AIC}_{\mathrm{eff}} > 2$ as support for the unbounded family. Where the n_{eff} estimate was not valid, $\Delta\mathrm{AIC}_{\mathrm{eff}}$ was recorded as missing rather than defaulting to the uncorrected value. The same deflation was applied to the partial models, $h(Y) \sim T_z + \mathrm{B}_z + \phi(\mathrm{CS}; \theta)$, using the residuals of the corresponding best unbounded partial fit; no permutation test was performed for these.

Spatial block cross-validation

Parametric adjustments for spatial autocorrelation can be sensitive to the assumed form of the correlogram, so we also compared the bounded and unbounded families by spatial block cross-validation, which assesses out-of-sample predictive performance without depending on λ [65]. Parcels were grouped into 10° × 10° blocks, and blocks were randomly assigned to 10 folds. Each fold was held out in turn: all candidate marginal models were refitted on the remaining blocks, with their non-linear parameters re-estimated on the training data, and used to predict richness in the held-out parcels. Folds with fewer than 20 test or 200 training parcels were skipped. Because whole blocks rather than individual parcels are withheld, training and test data are separated in space, which removes most of the optimism that spatial dependence introduces into parcel-wise cross-validation.

Predictions from log-scale models were back-transformed to the richness scale using Duan's smearing estimator [66], which corrects the retransformation bias that would otherwise penalise these models, and negative predictions were truncated at zero. Performance was summarised as the root mean square error (RMSE) of the pooled out-of-fold predictions on the original species-richness scale, so that models fitted on the log and identity scales are directly comparable without relying on the Jacobian correction. Models with fewer than 100 out-of-fold predictions were not scored. For each taxon and regime, the best unbounded and the best bounded model were identified by RMSE, and the family with the lower RMSE was recorded as the cross-validated winner.

Variance decomposition

To quantify the relative importance of deep-time environmental history versus contemporary climate and vegetation biomass density, we partitioned the explained variance of the partial richness models (Eq.17) using the Lindeman–Merenda–Gold (LMG) metric [67, 68]. For each

clade and regime, we took the best-fitting partial model selected by AIC. Holding $\boldsymbol{\psi}$ at its full-model estimate makes $\phi(\mathrm{CS};\boldsymbol{\psi})$ a fixed regressor, so the model is linear in its parameters and can be decomposed exactly by ordinary least squares over all subsets of the three predictors (T_z, B_z and ϕ). Because macroecological predictors are frequently collinear, a predictor's contribution to R^2 depends on the order in which it enters the model. LMG removes this dependence by averaging each predictor's sequential R^2 increment over all $3! = 6$ entry orderings, yielding order-independent shares that sum to the R^2 of the full model. We complemented LMG with a commonality analysis, which separates the variance explained uniquely by each predictor from that shared among them.

Spatial intersection with modern conservation networks

To evaluate whether present-day conservation networks protect regions with long histories of environmental stability, we intersected our modelled macroevolutionary refugia with protected areas and other effective area-based conservation measures (OECMs). We defined macroevolutionary refugia as land with CS > 20 Myr (**Methods** and **Supplementary Information**). Protected-area and OECM boundaries were obtained from the World Database on Protected Areas (WDPA) and the World Database on OECMs [36], downloaded from Protected Planet (https://www.protectedplanet.net) on 29 June 2026 and filtered to terrestrial and inland-water sites. Antarctica south of 60° S was excluded. Protected and total land area from a high-resolution reference grid were assigned to the nearest model cell within 125 km. Our gridded estimate of global terrestrial coverage (16.8% for protected areas alone and 17.9% including OECMs) agrees with the coverage published by Protected Planet (17.33%) to within 0.6 percentage points.

To account for differences in protection strictness, we evaluated the overlap across seven cumulative tiers of IUCN management categories:

- Tier 1: strict nature reserves and wilderness areas (Categories Ia and Ib).
- Tier 2: adding national parks (Categories I–II).
- Tier 3: adding natural monuments or features (Categories I–III).
- Tier 4: adding habitat and species management areas (Categories I–IV).
- Tier 5: adding protected landscapes and seascapes (Categories I–V).
- Tier 6: adding protected areas with sustainable use of natural resources (Categories I–VI).
- Tier 7: all sites, including protected areas without a reported IUCN category and OECMs.

Coverage was calculated as the fraction of refugia area falling within protected areas or OECMs at each tier. To assess geographic disparities, results were disaggregated into the seven Protected Planet regions: Africa, Asia, Europe, South America and the Caribbean, North America, Polar, and West Asia.

To propagate uncertainty in the model's biological parameters, we repeated the intersection for each of the 100,000 simulations, each with its own refugia mask. For each simulation, we computed the total refugia area and the area outside any protected area or OECM. We report the median of these 100,000 outcomes and their interquartile range (25th–75th percentiles), so that the reported protection gaps, globally and by region, reflect uncertainty in species' thermal breadths and environmental sensitivities.

Protection of stable versus unstable land across IUCN categories

To test whether macroevolutionary refugia are associated with greater conservation coverage, we partitioned all land cells (excluding Antarctica) into stable (CS > 20 Myr) and unstable (CS < 20 Myr) classes and compared their protected fractions across the seven cumulative IUCN tiers defined above. For each class c and tier t, coverage was calculated as the protected share of that class's total area,

$$\mathrm{cov}_{c,t} = 100 \times \frac{\sum_i m_{i,c}\, a_i\, f_{i,t}}{\sum_i m_{i,c}\, a_i} \tag{20}$$

where a_i is the land area of cell i, $f_{i,t}$ is its protected fraction at cumulative tier t, and $m_{i,c}$ is a binary membership indicator taking the value 1 if cell i belongs to class c and 0 otherwise.

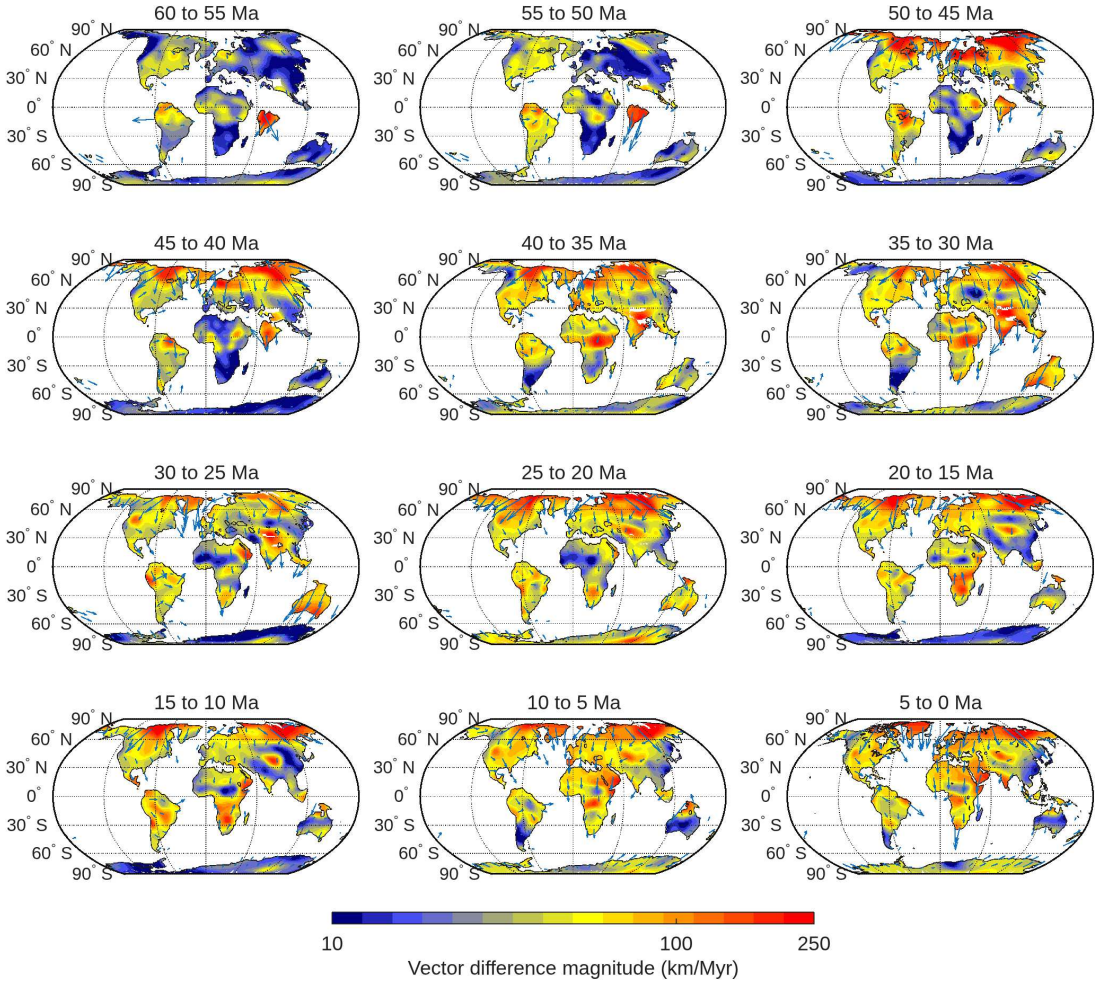
The protection gap was defined as the difference in coverage between the two classes, $\text{gap}_t = \text{cov}_{\text{stable},t} - \text{cov}_{\text{unstable},t}$, expressed in percentage points; a positive gap indicates that stable land is better protected than unstable land at that tier. We additionally computed the marginal contribution of each IUCN category as the first difference of coverage between consecutive tiers, which isolates how much each category adds to the coverage of each class.

Uncertainty was propagated from the full ensemble of 100,000 parameter combinations. We recomputed the stable/unstable partition independently within each simulation, and evaluated equation 20 separately for each. Central values are reported as the median across simulations of the statistic itself, with uncertainty as the 25^{th}–75^{th} percentiles of the same distribution. The gap was taken as the median of the per-simulation gap rather than the difference of the two medians, so reported gaps are not exactly additive with the reported coverages. As a non-parametric measure of consistency, we also report the proportion of simulations in which the gap was positive at each tier.

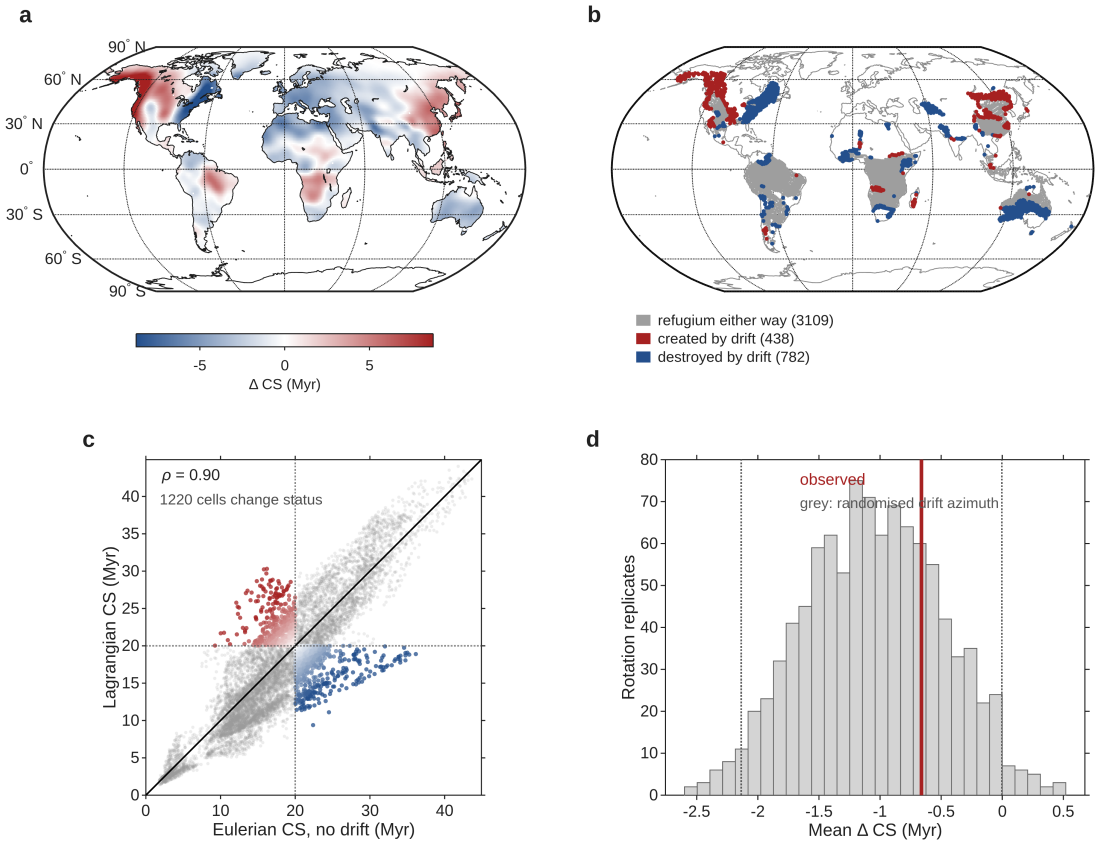
Protection priority index

The Protection Priority Index (PPI) was computed for each land grid cell i as the product of a stability value term and a protection shortfall term, $\text{PPI}_i = v_i^{\alpha} g_i^{\beta}$, with $\alpha = \beta = 1$. It can be read as the marginal conservation return of protecting an additional unit area in that cell. The value term $v_i \in [0, 1]$ is the area-weighted percentile rank of the cell's ensemble-mean cumulative stability (CS) among all retained land cells, obtained from an area-weighted empirical cumulative distribution function (mid-rank convention, linearly interpolated between nodes). Cells with zero land area or undefined CS were omitted, as were those within the Andean and Himalayan exclusion masks. The protection term $p_i \in [0, 1]$ was derived from WDPA coverage. We first isolated the fraction of each cell under each IUCN management category, $f_{i,k}$, assigning overlapping protected areas to the strictest category. We then summed these fractions weighted by an assumed effectiveness factor w_k (1.00 for categories Ia–Ib and II, 0.90 for III, 0.80 for IV, 0.50 for V and VI, and 0.25 for unassigned areas): $p_i = \min(1, \sum_k w_k f_{i,k})$. The protection shortfall is $g_i = 1 - p_i$. The PPI therefore ranges from 0 to 1 and is high only where land is both highly stable and poorly protected.

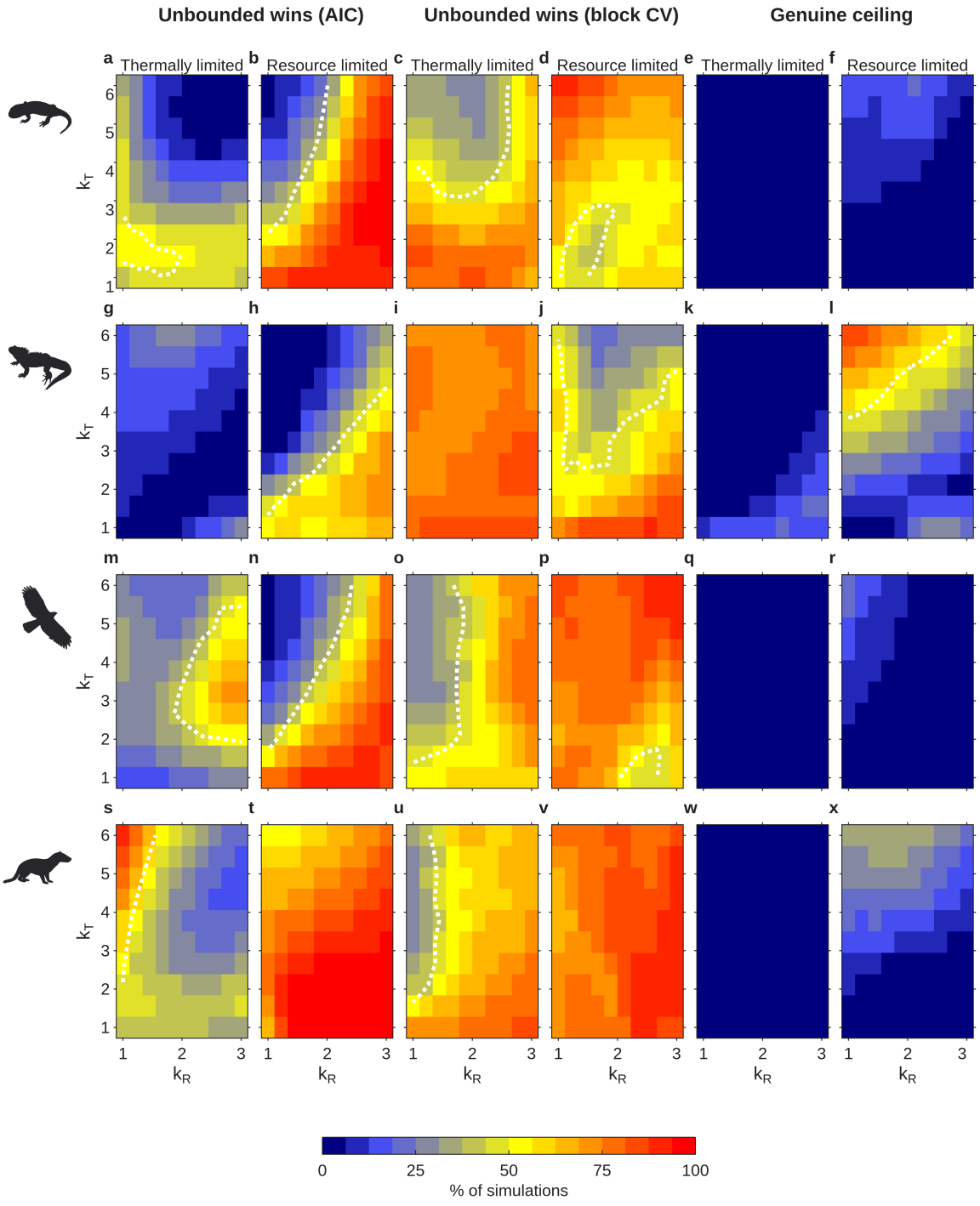
Regional PPI was computed as the area-weighted mean of cell values within each region; Antarctica was excluded from the global summary and from the regional ranking. To propagate stability uncertainty, the value transform was held fixed and the CS field of each of the 100,000 ensemble members was mapped through it; the shortfall term does not depend on CS and was held constant. Regional PPI is reported as the ensemble median and interquartile range. We tested the robustness of the regional ranking to the index's construction by recomputing it with greater weight on stability ($\alpha = 2$) or on the protection gap ($\beta = 2$), with protection restricted to categories I–IV, and with all protected areas weighted equally. For readability, PPI values in figures and tables are multiplied by 100.



Extended Data Figure 1: **Global vector difference maps between tectonic and climate velocities at 5 Myr time intervals spanning the last 60 Myr**. The arrows denote the net directional trajectory of the vector difference ($\mathbf{v}_{\text{diff}}$) and the underlying colour gradient represents the absolute magnitude of this divergence in km/Myr. A critical implication of this vector relationship is that thermal mismatch is maximized when tectonic and climate velocities are moving in opposite directions. Conversely, if a plate and its climate envelope are moving in the same direction at similar speeds, the resulting v_{diff} approaches zero, indicating a stable local environment despite high absolute global velocities.



Extended Data Figure 2: Plate motion reshapes terrestrial thermal refugia, with a net destabilising effect consistent with randomly oriented drift. Cumulative stability (CS) over the past 60 Myr was computed twice for every terrestrial cell, differing only in thermal forcing: the Lagrangian run uses the temperature change along each parcel's reconstructed trajectory ($|DT/Dt|$), the Eulerian run the change at its position had it not moved ($|\partial T/\partial t|$). The resource channel is identical, so $\Delta\mathrm{CS} = \mathrm{CS}_{\mathrm{Lagrangian}} - \mathrm{CS}_{\mathrm{Eulerian}}$ isolates the thermal effect of tectonic transport. **a**, ΔCS on a 1° grid masked to modern land, excluding Antarctica. Red, continental drift added stability; blue, drift removed it. Drift lowers CS on average (mean −0.65 Myr, IQR −2.63 to +1.03 Myr) but raises it in 39% of land cells. **b**, Refugium status under a 20 Myr threshold. Red cells qualify only because the parcel moved (3.91×10^6 km^2); blue cells would have qualified had it remained stationary (8.21×10^6 km^2), so continental drift removes about twice the area of refugia it creates. **c**, Cell-wise comparison against the 1:1 line, with cells that change status in colour. **d**, Null distribution of mean ΔCS from 1,000 replicates that preserve parcel speeds but randomise drift direction coherently in space and time; dotted lines mark its 95% interval (−2.14 to 0.00 Myr). The observed value (−0.66 Myr, red; two-sided $p = 0.51$) lies within it: the loss of stability is consistent with drift of the same speed in any direction, and its orientation relative to Cenozoic climate gradients is indistinguishable from random.



Extended Data Figure 3: **Sensitivity of the bounded versus unbounded verdict across the generalist–specialist continuum.** Each panel shows the percentage of simulations in the parameter ensemble meeting a given criterion, as a function of thermal sensitivity (k_T, vertical axis) and resource sensitivity (k_E, horizontal axis); low values denote generalists and high values specialists. Rows are taxa (top to bottom: amphibians, reptiles, birds, mammals). Column pairs correspond to three criteria: the AIC verdict on the marginal fits (**a**–**b**, **g**–**h**, **m**–**n**, **s**–**t**), the spatial block cross-validation verdict (**c**–**d**, **i**–**j**, **o**–**p**, **u**–**v**), and the proportion of simulations showing a genuine ceiling, defined as a bounded win accompanied by saturation within the observed stability range (**e**–**f**, **k**–**l**, **q**–**r**, **w**–**x**). Within each pair the left panel is the thermally limited regime and the right panel the resource-limited regime. White dotted lines mark the 50% isoline, at which the two model families are selected equally often.

Extended Data Table 1: Variables, parameters and units

Symbol	Description	Units	Value / range
Velocities and thermal rates			
$\mathbf{v}_{\text{tec}}$	Plate (tectonic) velocity	km Myr^{-1}	–
$\mathbf{v}_{\text{clim}}$	Climate velocity (isotherm displacement)	km Myr^{-1}	–
$\mathbf{v}_{\text{diff}}$	Velocity difference, $\mathbf{v}_{\text{clim}} - \mathbf{v}_{\text{tec}}$	km Myr^{-1}	–
∇T	Spatial temperature gradient	$^{\circ}\text{C km}^{-1}$	–
$\partial T/\partial t$	Eulerian rate of temperature change	$^{\circ}\text{C Myr}^{-1}$	–
DT/Dt	Lagrangian rate of temperature change (signed thermal mismatch)	$^{\circ}\text{C Myr}^{-1}$	–
ΔT_i	Temperature change over a step	$^{\circ}\text{C}$	–
$\mathcal{L}$	Kinematic lag	km Myr^{-1}	–
Biological capacities (conceptual framework only)			
V_{disp}	Dispersal velocity	km Myr^{-1}	0^a
r_{adpt}	Rate of thermal adaptation	$^{\circ}\text{C Myr}^{-1}$	0^a
Thermal stability			
S_i	Instantaneous thermal stability	–	0–1
$\Delta T_{\text{breadth}}$	Representative thermal niche breadth	$^{\circ}\text{C}$	2–10
k_T	Thermal sensitivity constant	–	1–6
Resources			
$B_i(t)$	Vegetation biomass density	g C m^{-2}	–
B_{95}	95th percentile of B (all parcels and steps)	g C m^{-2}	–
$\Delta B_i(t)$	Biomass change over a step	g C m^{-2}	–
$\delta_i(t)$	Relative biomass decline	–	–
ρ	Resilience tolerance (fraction of prior biomass)	–	0–0.1
$\Delta B_i^{\text{loss}}(t)$	Biomass decline beyond tolerance	g C m^{-2}	–
k_R	Resource sensitivity constant	–	$1–3^b$
R_i	Resource retention factor	–	0–1
B_{thresh}	Ecological capacity threshold	g C m^{-2}	$(0.15–0.23)\, B_{95}$
$\min(1, B_i/B_{\text{thresh}})$	Ecological capacity limit	–	0.01–1
Stability metrics			
$\text{IS}_i(t)$	Interval stability gain	Myr	0–5
$\text{CS}_i(t)$	Cumulative stability	Myr	0–60

Notes: Bold symbols denote horizontal vectors; – in the Units column denotes a dimensionless quantity. $\Delta B_i(t) = B_i(t) - B_i(t - \Delta t)$; $\delta_i(t) = -\Delta B_i(t)/B_i(t - \Delta t)$; $\text{IS}_i(t) = S_i \min(1, B_i/B_{\text{thresh}})\, \Delta t$. Ranges for $\Delta T_{\text{breadth}}$, k_T, k_R, ρ and the B_{thresh} fraction were each sampled at ten values (100,000 combinations); reported CS values are ensemble means. [a]Set to zero in all analyses, for which $\mathcal{L}\,|\nabla T| = |DT/Dt|$. [b]Log-spaced; all other ranges linearly spaced.

Extended Data Table 2: Marginal $Y \sim \phi(S)$ – the bounded vs unbounded test. $\Delta\text{AIC} > 0$ favours unbounded. $\Delta\text{AIC}_{\text{eff}}$ applies the spatial deflation $\lambda = n_{\text{eff}}/n$.

Taxon	n	Best unbounded	Best bounded	ΔAIC	$\Delta\text{AIC}_{\text{eff}}$	CV winner
Thermally limited						
Amphibians	3886	lg_Exponential	lg_Logistic	−90.5	−0.3	bounded
Reptiles	4222	lg_Exponential	lg_Logistic	−220.7	−0.6	unbounded
Birds	4237	id_Power	id_Logistic	−24.2	−0.1	unbounded
Mammals	4222	lg_Exponential	lg_Logistic	−102.8	−0.3	bounded
Resource limited						
Amphibians	4706	lg_Exponential	lg_Monomolec	+2.5	+0.0	unbounded
Reptiles	6239	lg_Power	lg_MichMenten	−41.9	−0.1	unbounded
Birds	6201	id_Exponential	id_Logistic	+3.8	+0.0	unbounded
Mammals	6239	lg_Power	lg_MichMenten	+38.8	+0.1	bounded

Extended Data Table 3: Is a bounded win actually evidence of a ceiling?

Taxon	AIC says	Best bounded	satFrac	bounded shape	unbounded shape	
Thermally limited						
Amphibians	bounded	lg_Logistic	0.89	accelerating	accelerating	← no ceiling in range
Reptiles	bounded	lg_Logistic	1.00	accelerating	accelerating	← no ceiling in range
Birds	bounded	id_Logistic	0.77	accelerating	accelerating	← no ceiling in range
Mammals	bounded	lg_Logistic	0.89	accelerating	accelerating	← no ceiling in range
Resource limited						
Amphibians	unbounded	lg_Monomolec	0.05	accelerating	accelerating	
Reptiles	bounded	lg_MichMenten	0.81	accelerating	accelerating	← no ceiling in range
Birds	unbounded	id_Logistic	0.51	accelerating	accelerating	
Mammals	unbounded	lg_MichMenten	0.75	decelerating	decelerating	

Extended Data Table 4: Variance decomposition and commonality components of the selected partial models. LMG shares are % of explained variance, while commonality components are in absolute R^2 units.

	Thermally limited				**Resource limited**			
Metric	**Amph.**	**Rept.**	**Birds**	**Mamm.**	**Amph.**	**Rept.**	**Birds**	**Mamm.**
Model Specifications								
Model	lg_Logistic	lg_Logistic	id_Logistic	lg_Logistic	lg_Expon.	lg_Power	id_Logistic	lg_MichM.
Scale	log	log	identity	log	log	log	identity	log
R^2_{tot}	0.716	0.849	0.600	0.567	0.413	0.782	0.418	0.421
LMG / Shapley Variance (%)								
Time	13.6	20.3	30.6	34.3	31.4	31.8	41.3	41.7
Temp	45.6	53.8	25.6	23.7	21.2	55.3	11.8	15.9
Biomass	40.8	25.9	43.8	42.1	47.5	12.9	46.9	42.4
Commonality Components (absolute R^2)								
U(Time)	0.007	0.003	0.044	0.034	0.030	0.015	0.067	0.087
U(Temp)	0.084	0.218	0.005	0.001	0.015	0.196	0.001	0.004
U(Biomass)	0.044	0.004	0.079	0.064	0.110	0.008	0.097	0.108
Shared	0.580	0.624	0.472	0.468	0.260	0.564	0.254	0.223
C(T,N)	0.321	0.142	0.095	0.035	0.015	0.014	0.000	−0.004
C(T,Time)	0.007	0.050	0.006	0.007	0.042	0.298	0.013	0.033
C(N,Time)	0.016	0.004	0.076	0.091	0.069	0.010	0.114	0.047
C(all)	0.237	0.428	0.294	0.335	0.133	0.241	0.126	0.147

Extended Data Table 5: Global land and protection statistics

	Total		**Stable land characteristics**							
Region	Land (Mkm^2)	Prot. (%)	Land (Mkm^2)	p25	p75	Prot. (%)	Unprot. (%)	Unprot. area (Mkm^2)	Unprot. Q1	Unprot. Q3
Global	128.5	17.8	42.2	22.2	66.7	22.1	77.9	32.86	16.02	53.15
Asia	42.3	11.4	10.9	4.8	19.2	8.5	91.5	9.96	4.48	16.71
Africa	30.2	19.4	11.6	7.2	17.3	22.5	77.5	8.99	5.36	13.65
South America & Caribbean	17.6	35.4	12.7	8.7	16.1	38.2	61.8	7.88	4.81	10.30
North America	21.2	13.5	6.5	1.6	13.2	12.2	87.8	5.73	1.34	11.66
Polar	3.2	30.1	0.0	0.0	0.0	–	–	0.00	0.00	0.00
West Asia	8.4	10.8	0.0	0.0	1.0	–	–	0.00	0.00	0.88
Europe	5.5	22.6	0.0	0.0	0.0	–	–	0.00	0.00	0.01

Extended Data Table 6: Distribution by protection categories (total vs. stable)

	Total categories							Stable categories						
Region	**I**	**II**	**III**	**IV**	**V**	**VI**	**Other**	**I**	**II**	**III**	**IV**	**V**	**VI**	**Other**
Global	1.7	3.7	0.2	1.5	1.4	3.3	5.9	2.1	4.8	0.3	1.0	1.7	4.5	7.7
Asia	1.6	2.0	0.2	1.5	0.3	4.0	1.8	1.0	2.5	0.2	0.7	0.5	2.5	1.1
Africa	0.6	3.3	0.1	2.4	0.2	2.2	10.7	0.7	6.3	0.1	2.2	0.3	4.5	8.5
South America & Caribbean	2.0	6.0	0.8	0.5	5.2	7.0	14.0	2.7	6.4	0.9	0.4	4.2	7.8	15.9
North America	4.2	3.3	0.1	1.1	1.2	1.3	2.3	4.1	3.0	0.0	0.6	1.5	0.7	2.1
Polar	0.6	29.2	0.0	0.2	0.0	0.0	0.1	–	–	–	–	–	–	–
West Asia	0.4	1.5	0.0	1.2	0.6	4.9	2.3	–	–	–	–	–	–	–
Europe	1.6	1.8	0.1	3.0	6.6	0.3	9.3	–	–	–	–	–	–	–

Extended Data Table 7: Ensemble uncertainty on the stable-land result (per-simulation median [p25 – p75] across 100,000 simulations).

Metric / IUCN category	**Median**	**IQR [p25 – p75]**
Total stable area (M km^2)	**42.16**	**[22.24 – 66.73]**
Protected area distribution (%)		
Cat Ia+Ib (strict)	2.1	[2.0 – 2.2]
Cat I–II	6.9	[6.3 – 8.2]
Cat I–III	7.2	[6.6 – 8.7]
Cat I–IV	8.2	[7.7 – 9.8]
Cat I–V	9.9	[9.5 – 11.3]
Cat I–VI	14.5	[13.7 – 17.2]
All (incl. uncategorised)	22.1	[20.3 – 27.9]

Extended Data Table 8: **Regional protection priority and sensitivity of the regional ranking.** Land area, mean cumulative stability (CS) and protection coverage for each region, with the protection priority index averaged over the region's land, weighted by area.

			Protected (%)		Ensemble PPI		PPI (rank) under alternative index settings				
Region	Land (M km^2)	Mean CS (Myr)	All	Effective	Median [IQR]	Rank	Baseline	$\alpha = 2$	$\beta = 2$	I–IV only	All equal
Global (excl. Polar)	121.6	17.5	17.8	10.4	43.7 [30.2–57.3]	–	–	–	–	–	–
South America & Caribbean	16.7	25.8	36.9	19.5	61.4 [50.5–69.1]	1	61.9 (1)	50.2 (1)	53.0 (1)	69.7 (1)	47.7 (1)
Africa	30.2	18.7	19.4	9.7	47.7 [34.9–59.8]	2	49.0 (2)	33.8 (2)	45.2 (2)	51.0 (2)	44.0 (**3**)
North America	21.2	16.5	13.5	10.3	44.4 [26.9–59.0]	3	45.8 (3)	29.1 (3)	42.5 (3)	46.6 (3)	44.3 (**2**)
Asia	39.7	15.8	11.7	7.8	40.4 [26.7–55.4]	4	42.1 (4)	26.2 (4)	39.6 (4)	43.2 (4)	40.4 (4)
West Asia	8.4	12.4	10.8	6.1	26.8 [12.5–46.0]	5	29.6 (5)	10.5 (5)	28.3 (5)	30.5 (5)	28.3 (5)
Europe	5.5	9.4	22.6	11.6	13.7 [5.5–32.3]	6	17.3 (6)	4.3 (6)	15.4 (6)	18.6 (6)	14.7 (6)
Polar	3.2	3.5	30.1	30.0	2.3 [0.7–6.8]	–	–	–	–	–	–

Notes: Protected, all: share of land within any protected area or OECM [36]. *Protected, effective*: the same share with IUCN categories weighted by assumed management effectiveness (**Methods**). *Ensemble PPI*: median and interquartile range (25th–75th percentiles) across the simulation ensemble; regions are ranked by the median. *Alternative index settings*: regional PPI and rank (in parentheses) recomputed from a single CS field (the cell-wise ensemble median) under the baseline index and four alternatives: stability term squared ($\alpha = 2$), shortfall term squared ($\beta = 2$), only Categories I–IV counted as protected, and all categories weighted equally. Bold ranks differ from the baseline. The Andes and Himalayas are excluded throughout; Polar land is excluded from the global row and the ranking.

References

[1] Kent, D. V. & Muttoni, G. Equatorial convergence of India and early Cenozoic climate trends. *Proceedings of the National Academy of Sciences* **105**, 16065–16070 (2008).

[2] Goddéris, Y., Donnadieu, Y., Le Hir, G., Lefebvre, V. & Nardin, E. The role of palaeogeography in the Phanerozoic history of atmospheric CO_2 and climate. *Earth-Science Reviews* **128**, 122–138 (2014).

[3] Zahirovic, S., Müller, R. D., Seton, M. & Flament, N. Tectonic speed limits from plate kinematic reconstructions. *Earth and Planetary Science Letters* **418**, 40–52 (2015).

[4] Scotese, C. R. An atlas of Phanerozoic paleogeographic maps: The seas come in and the seas go out. *Annual Review of Earth and Planetary Sciences* **49**, 679–728 (2021).

[5] Westerhold, T. *et al.* An astronomically dated record of Earth's climate and its predictability over the last 66 million years. *Science* **369**, 1383–1388 (2020).

[6] Loarie, S. R. *et al.* The velocity of climate change. *Nature* **462**, 1052–1055 (2009). URL https://doi.org/10.1038/nature08649.

[7] Burrows, M. T. *et al.* The pace of shifting climate in marine and terrestrial ecosystems. *Science* **334**, 652–655 (2011).

[8] Valentine, J. W. & Moores, E. M. Plate-tectonic regulation of faunal diversity and sea level: A model. *Nature* **228**, 657–659 (1970).

[9] Pellissier, L., Heine, C., Rosauer, D. F. & Albouy, C. Are global hotspots of endemic richness shaped by plate tectonics? *Biological Journal of the Linnean Society* **123**, 247–261 (2017).

[10] Couvreur, T. L. P. *et al.* Tectonics, climate and the diversification of the tropical African terrestrial flora and fauna. *Biological reviews of the Cambridge Philosophical Society* **96**, 16–51 (2021).

[11] MacArthur, R. & Wilson, E. *The Theory of Island Biogeography.* (Princeton University Press, Princeton, 1967).

[12] Whittaker, R. J., Triantis, K. A. & Ladle, R. J. A general dynamic theory of oceanic island biogeography. *Journal of Biogeography* **35**, 977–994 (2008).

[13] Weigelt, P., Steinbauer, M. J., Cabral, J. S. & Kreft, H. Late Quaternary climate change shapes island biodiversity. *Nature* **532**, 99–102 (2016).

[14] Jetz, W., Peet-Pare, C. A. & Rahbek, C. Global gradients in vertebrate diversity predicted by historical area-productivity dynamics and contemporary environment. *PLoS Biology* **10**, e1001292 (2012).

[15] Jansson, R. Global patterns in endemism explained by past climatic change. *Proceedings of the Royal Society of London. Series B: Biological Sciences* **270**, 583–590 (2003).

[16] Carnaval, A. C., Hickerson, M. J., Haddad, C. F. B., Rodrigues, M. T. & Moritz, C. Stability predicts genetic diversity in the Brazilian Atlantic forest hotspot. *Science* **323**, 785–789 (2009).

[17] Sandel, B. *et al.* The influence of late quaternary climate-change velocity on species endemism. *Science* **334**, 660–664 (2011).

[18] Harrison, S. & Noss, R. Endemism hotspots are linked to stable climatic refugia. *Annals of Botany* **119**, 207–214 (2017).

[19] Close, R. A., Benson, R. B. J., Saupe, E. E., Clapham, M. E. & Butler, R. J. The spatial structure of phanerozoic marine animal diversity. *Science* **368**, 420–424 (2020).

[20] Kocsis, Á. T. & Scotese, C. R. Mapping paleocoastlines and continental flooding during the Phanerozoic (2021). URL https://doi.org/10.1016/j.earscirev.2020.103463https://www.sciencedirect.com/science/article/pii/S0012825220305092?via%3Dihub.

[21] Jones, L. A. *et al.* palaeoverse: A community-driven R package to support palaeobiological analysis. *Methods in Ecology and Evolution* **14**, 2205–2215 (2023).

[22] Ree, R. H. & Smith, S. A. Maximum likelihood inference of geographic range evolution by dispersal, local extinction, and cladogenesis. *Systematic Biology* **57**, 4–14 (2008).

[23] Ronquist, F. & Sanmartín, I. Phylogenetic methods in biogeography. *Annual Review of Ecology, Evolution, and Systematics* **42**, 441–464 (2011).

[24] Merdith, A. S. *et al.* Extending full-plate tectonic models into deep time: Linking the Neoproterozoic and the Phanerozoic. *Earth-Science Reviews* **214**, 103477 (2021).

[25] Matthews, K. J. *et al.* Global plate boundary evolution and kinematics since the late Paleozoic. *Global and Planetary Change* **146**, 226–250 (2016).

[26] Vérard, C. 888–444 Ma Global Plate Tectonic Reconstruction With Emphasis on the Formation of Gondwana. *Frontiers in Earth Science* **9** (2021).

[27] Cermeño, P. *et al.* Post-extinction recovery of the Phanerozoic oceans and biodiversity hotspots. *Nature* **607**, 507–511 (2022). URL 10.1038/s41586-022-04932-6.

[28] Schloss, C. A., Nuñez, T. A. & Lawler, J. J. Dispersal will limit ability of mammals to track climate change in the Western Hemisphere. *Proceedings of the National Academy of Sciences of the United States of America* **109**, 8606–8611 (2012).

[29] Lenoir, J. *et al.* Species better track climate warming in the oceans than on land. *Nature Ecology & Evolution* **4**, 1044–1059 (2020).

[30] Román-Palacios, C. & Wiens, J. J. Recent responses to climate change reveal the drivers of species extinction and survival. *Proceedings of the National Academy of Sciences* **117**, 4211–4217 (2020).

[31] Tilman, D., May, R. M., Lehman, C. L. & Nowak, M. A. Habitat destruction and the extinction debt. *Nature* **371**, 65–66 (1994).

[32] Gurung, K., Field, K. J., Batterman, S. A., Poulton, S. W. & Mills, B. J. W. Geographic range of plants drives long-term climate change. *Nature Communications* **15**, 1805 (2024).

[33] Jenkins, C. N., Pimm, S. L. & Joppa, L. N. Global patterns of terrestrial vertebrate diversity and conservation. *Proceedings of the National Academy of Sciences* **110**, E2602–E2610 (2013).

[34] Roll, U. *et al.* The global distribution of tetrapods reveals a need for targeted reptile conservation. *Nature Ecology & Evolution* **1**, 1677–1682 (2017).

[35] Caetano, G. H. d. O. *et al.* Automated assessment reveals that the extinction risk of reptiles is widely underestimated across space and phylogeny. *PLOS Biology* **20**, e3001544 (2022).

[36] UNEP-WCMC and IUCN. Protected planet: The world database on protected areas (WDPA) and world database on OECMs. https://www.protectedplanet.net (2026). Accessed August 2026.

[37] Benton, M. J. The Red Queen and the Court Jester: Species diversity and the role of biotic and abiotic factors through time. *Science* **323**, 728–732 (2009).

[38] Rabosky, D. L. & Hurlbert, A. H. Species richness at continental scales is dominated by ecological limits. *The American Naturalist* **185**, 572–583 (2015).

[39] Harmon, L. J. & Harrison, S. Species diversity is dynamic and unbounded at local and continental scales. *The American Naturalist* **185**, 584–593 (2015).

[40] Dynesius, M. & Jansson, R. Persistence of within-species lineages: a neglected control of speciation rates. *Evolution; international journal of organic evolution* **68**, 923–934 (2014).

[41] Davis, M., Faurby, S. & Svenning, J.-C. Mammal diversity will take millions of years to recover from the current biodiversity crisis. *Proceedings of the National Academy of Sciences* **115**, 11262–11267 (2018).

[42] Buckley, L. B., Hurlbert, A. H. & Jetz, W. Broad-scale ecological implications of ectothermy and endothermy in changing environments. *Global Ecology and Biogeography* **21**, 873–885 (2012).

[43] Rolland, J. *et al.* The impact of endothermy on the climatic niche evolution and the distribution of vertebrate diversity. *Nature Ecology & Evolution* **2**, 459–464 (2018).

[44] Purvis, A., Agapow, P.-M., Gittleman, J. L. & Mace, G. M. Nonrandom extinction and the loss of evolutionary history. *Science* **288**, 328–330 (2000). URL https://www.science.org/doi/10.1126/science.288.5464.328.

[45] Convention on Biological Diversity. Kunming-montreal global biodiversity framework. Decision adopted by the Conference of the Parties to the Convention on Biological Diversity, 15/4 CBD/COP/DEC/15/4, Secretariat of the Convention on Biological Diversity, Montreal, Canada (2022). URL https://www.cbd.int/doc/decisions/cop-15/cop-15-dec-04-en.pdf.

[46] Svenning, J.-C., Eiserhardt, W. L., Normand, S., Ordonez, A. & Sandel, B. The Influence of Paleoclimate on Present-Day Patterns in Biodiversity and Ecosystems. *Annual Review of Ecology, Evolution, and Systematics* **46**, 551–572 (2015). URL http://www.jstor.org/stable/24810162.

[47] Kuussaari, M. *et al.* Extinction debt: a challenge for biodiversity conservation. *Trends in Ecology & Evolution* **24**, 564–571 (2009).

[48] McGuire, J. L., Lawing, A. M., Díaz, S. & Stenseth, N. C. The past as a lens for biodiversity conservation on a dynamically changing planet. *Proceedings of the National Academy of Sciences* **120**, e2201950120 (2023).

[49] Anderson, M. G. *et al.* A resilient and connected network of sites to sustain biodiversity under a changing climate. *Proceedings of the National Academy of Sciences* **120**, e2204434119 (2023).

[50] Rahbek, C. *et al.* Building mountain biodiversity: Geological and evolutionary processes. *Science* **365**, 1114–1119 (2019).

[51] Salles, T., Husson, L., Lorcery, M. & Hadler Boggiani, B. Landscape dynamics and the phanerozoic diversification of the biosphere. *Nature* **624**, 115–121 (2023).

[52] Scotese, C. R. & Wright, N. Paleomap paleodigital elevation models (paleodems) for the phanerozoic. PALEOMAP Project (2018). URL https://www.earthbyte.org/paleodem-resource-scotese-and-wright-2018/.

[53] Mills, B. J., Donnadieu, Y. & Goddéris, Y. Spatial continuous integration of phanerozoic global biogeochemistry and climate. *Gondwana Research* **100**, 73–86 (2021).

[54] Sitch, S. *et al.* Evaluation of ecosystem dynamics, plant geography and terrestrial carbon cycling in the LPJ dynamic global vegetation model. *Global Change Biology* **9**, 161–185 (2003).

[55] Zelinka, M. D. *et al.* Causes of higher climate sensitivity in CMIP6 models. *Geophysical Research Letters* **47**, e2019GL085782 (2020).

[56] Jenks, G. F. The data model concept in statistical mapping. *International Yearbook of Cartography* **7**, 186–190 (1967).

[57] Otsu, N. A threshold selection method from gray-level histograms. *IEEE Transactions on Systems, Man, and Cybernetics* **9**, 62–66 (1979).

[58] Running, S. W. & Zhao, M. Mod17a3hgf modis/terra net primary production gap-filled yearly l4 global 500 m sin grid v006 (2019). URL https://doi.org/10.5067/MODIS/MOD17A3HGF.006. Accessed: 2026-09-25.

[59] IUCN. The IUCN red list of threatened species. version 2018-1 (2018). URL https://www.iucnredlist.org.

[60] Rabosky, D. L. Diversity-dependence, ecological speciation, and the role of competition in macroevolution. *Annual Review of Ecology, Evolution, and Systematics* **44**, 481–502 (2013).

[61] Burnham, K. P. & Anderson, D. R. *Model Selection and Multimodel Inference: A Practical Information-Theoretic Approach* 2nd edn (Springer Science & Business Media, 2002).

[62] Diniz-Filho, J. A. F., Bini, L. M. & Hawkins, B. A. Spatial autocorrelation and red herrings in geographical ecology. *Global Ecology and Biogeography* **12**, 53–64 (2003). URL https://onlinelibrary.wiley.com/doi/abs/10.1046/j.1466-822X.2003.00322.x.

[63] Griffith, D. A. & Plant, R. E. Statistical analysis in the presence of spatial autocorrelation: Selected sampling strategy effects. *Stats* **5**, 1334–1353 (2022). URL https://doi.org/10.3390/stats5040081.

[64] Clifford, P., Richardson, S. & Hémon, D. Assessing the significance of the correlation between two spatial processes. *Biometrics* **45**, 123–134 (1989).

[65] Roberts, D. R. *et al.* Cross-validation strategies for data with temporal, spatial, hierarchical, or phylogenetic structure. *Ecography* **40**, 913–929 (2017).

[66] Duan, N. Smearing estimate: A nonparametric retransformation method. *Journal of the American Statistical Association* **78**, 605–610 (1983).

[67] Lindeman, R. H., Merenda, P. F. & Gold, R. Z. *Introduction to Bivariate and Multivariate Analysis* (Scott, Foresman, Glenview, IL, 1980).

[68] Groemping, U. Relative importance for linear regression in R: The package relaimpo. *Journal of Statistical Software* **17**, 1–27 (2006). URL https://doi.org/10.18637/jss.v017.i01.

Acknowledgements. FOAM simulations were performed using HPC resources from DNUM CCUB (Centre de Calcul de l'Université de Bourgogne).

Declarations

- Funding – This work was funded by research grant PID2023-152076NB-I00 (project INDI-CiOS) from the Spanish government and the French Agence Nationale de la Recherche (ANR) under reference ANR-22-CE01-0003 (project ECO-BOOST).

- The authors have no conflicts of interest to declare.

- Data availability. All data required to reproduce the analyses are available for peer review at https://anonymous.4open.science/r/deep-time-environmental-stability-model-C8E7/README.md and will be archived at Zenodo upon acceptance. It includes processed outputs derived from the following publicly available sources: plate tectonic reconstructions from Merdith et al. [24] (https://doi.org/10.5281/zenodo.13635864); palaeotopography from the PALEOMAP project [52]; species richness maps from BiodiversityMapping.org [33] (https://biodiversitymapping.org), derived from range maps from the IUCN Red List of Threatened Species [59], BirdLife International (https://datazone.birdlife.org/), and the Global Assessment of Reptile Distributions [34]; and protected-area boundaries from the World Database on Protected Areas (UNEP-WCMC and IUCN, June 2026, https://www.protectedplanet.net). The SCION–FLORA palaeoclimate simulations used in this study were generated specifically for this work using the models described in refs [32, 53].

- Supplementary Information is available for this paper.

- Code availability. The code to reproduce the analyses, tables and figures in this study is available for peer review at https://anonymous.4open.science/r/deep-time-environmental-stability-model-C8E7/README.md and will be archived at Zenodo upon acceptance.

- Author contribution. P.C. conceived the study. P.C., C.G.C, A.P, B.M, and K.G. designed the analyses. S.W. built the palaeogeographic model. A.P. and G.H-G. performed the FOAM climate simulations. B.M. and K.G. performed the SCION–FLORA simulations forced by the FOAM outputs. P.C., C.G-C., G.H-G., and G.L.G developed the Lagrangian framework and carried out the analyses with the help of all authors. P.C. wrote the manuscript with input from all authors. All authors discussed the results and commented on the manuscript.

Correspondence and requests for materials should be addressed to pedrocermeno@icm.csic.es.

Supplementary Files

This is a list of supplementary files associated with this preprint. Click to download.

- cermenoetalSI.pdf